9-2024

Theoretical and Experimental Study of Thermoradiative Cells for Space Power Generation

Andrew Schaefer
als6934@rit.edu

RIT College of Science School of Physics and Astronomy

Theoretical and Experimental Study of Thermoradiative Cells for Space Power Generation

By

ANDREW SCHAEFER

A Thesis Submitted in partial fulfillment of the requirements for the degree of Masters of Science in Physics in the

School of Physics and Astronomy
College of Science
Rochester Institute of Technology
Rochester, NY

September 2024

Approved by:_____

George Thurston, Ph.D Date
Director, Physics

RIT | College of Science
School of Physics and Astronomy
ROCHESTER, NEW YORK

CERTIFICATE OF APPROVAL

MASTER'S DEGREE THESIS

The Master's Degree Thesis of Andrew Schaefer has been examined and approved by the thesis committee as satisfactory for the thesis requirement for the Master's degree in Physics

Dr. Seth Hubbard, Thesis Advisor

Dr. Pratik Dholabhai, Committee Member

Dr. Michael Pierce, Committee Member

Dr. Stephen Polly , Committee Member

Date _____

Acknowledgements

A special thank you too all below. Without you this project would not have been possible.

- Dr. Stephen Polly
- Dr. Seth Hubbard
- Members of committee: Dr. Michael Pierce, Dr. Pratik Dholabhai
- Ross Hisert
- NPRL Ph. D. Candidate Elijah Sacchitella

Abstract

Reliable power production is always a core element when engineers design a space mission. Typically, III-V solar arrays are used due to their high efficiency, radiation tolerance, and overall reliability. One downside of photovoltaics involves the need for incident light from the Sun. There are many places in the solar system and beyond that do not have access to sustained, high concentration solar radiation. As missions fly farther from the Sun, the available light power decreases with the inverse square of the distance. This means that missions past Jupiter are only receiving one tenth the solar power compared to Earth. In these scenarios, power can be produced by converting the heat from a radioisotope using thermoelectric devices. This study will demonstrate experimentally and theoretically that heat can be converted using another device named a thermoradiative cell (TRC). This cell is heated above the temperature of the ambient which causes a net flow of photons out of the cell. To sustain this, electrons from the circuit must be pulled in which causes a current to flow. This project explored this mechanism by using detailed balance calculations to predict an upper limit power and current generation as well as some loss mechanisms. An experiment was also conducted to demonstrate this effect under space-like conditions and a measure power was produced.

Table of Contents

Table of Figures

1 Introduction

1.1 Background

Most space missions utilize photovoltaic arrays to generate the necessary power. Photovoltaics are great in many scenarios but lack capabilities if sunlight is not present. There are many places in the Solar System worth exploring that are devoid of sunlight. For example, the icy giants Uranus and Neptune are a hot topic of exploration. Figure 1 shows the available solar power for each planet. At 20 or 30 astronomical units the available solar power form the Sun has reduced by over a factor of 100. This reduction in input energy from the Sun will dramatically reduce the power production of a solar array.

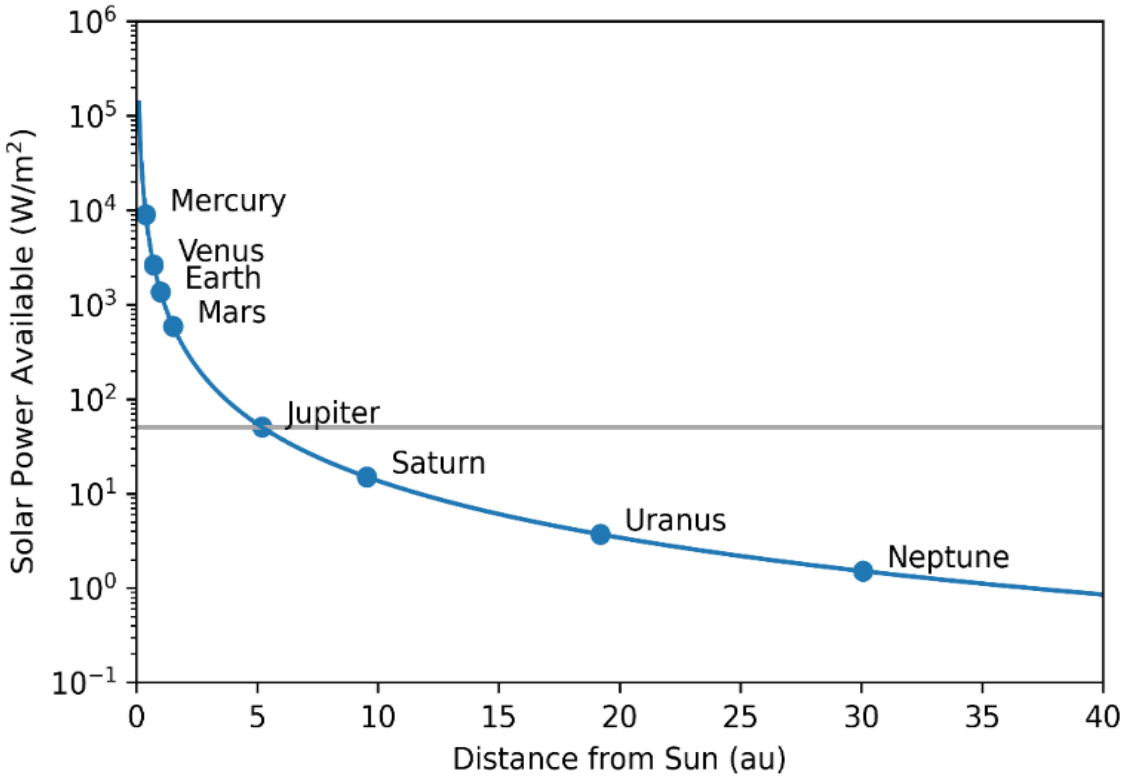

Figure 1 A plot of the available Solar Power at each planet due to the Inverse Square Law

Additionally, different bodies have areas that are completely blocked from the Sun, such as moon craters. Photovoltaics are completely unusable in these regions. This necessitates the need for different power generation methods. Figure 2 shows the Multi-Mission Radioisotope Thermal Generator (MMRTG). This system converts the heat generated by the radioactive decay of Plutonium into electrical power using thermoelectric devices. Cooling fins on the exterior radiate away heat from the cold side of the thermoelectric devices to maintain a temperature difference across the device. This type of system was used on many missions including both Mars rovers as well as NASA Dragonfly with the potential to be used on many more.

Figure 2 Multi-Mission Radioisotope Thermal Generator used by NASA capable of generating 110 Watts of electrical power.

While these RTGs unlock new regions of our Solar System for exploration, they do come with some costs. These systems are large, heavy, and somewhat unwieldy with bulky cooling fins required to maintain the temperature difference across the thermoelectric devices. Additionally, the RTG beginning of life efficiency is only 6% [1]. This project studies Thermoradaitive Cells (TRCs), a novel device that can be used in combination with or replace the thermoelectrics currently in the system, and possibly provide more power to these systems with no need for sunlight.

The first efficiency calculations for TRCs were completed in 2015 by Rune Strandberg in [2], and the number of citations and publications on this topic has only increased since. There have also been groups that have demonstrated the thermoradiative effect in their labs, but only for temperature differences that are found terrestrially. First, the Nielson & Ekins-Daukes et al. demonstrated a maximum power production of 2.26 mW/cm^2 with a temperature difference of 12.5 °C using a Mercury Cadmium Telluride (HgCdTe) photodiode [3]. Next, Ono, Fan et al. was able to produce a maximum power of 6.39×10^{-7} mW/cm^2 using the night sky as a cold sink with a room temperature HgCdTe diode [4]. Lastly, the Fan group produced a maximum generated power of 10^{-6} mW/cm^2 with a temperature difference of 10 °C and a HgCdTe photodiode [5]. These experimental studies demonstrate Thermoradiative power generation for terrestrial temperatures. This study aims to demonstrate the practicality of TRCs for space use both theoretically and experimentally.

1.2 General Thermoradiative Concept

The basic workings of a TRC are not inherently different from a typical solar cell and theoretically, under the right conditions a typical solar cell could demonstrate the

thermoradiative effect. All that would need to change is the cell's field of view or its own temperature. Figure 3 compares energy transfer between a thermoradiative cell and a photovoltaic (PV) cell. At a high level, a PV cell converts an input of light to heat and electrical energy. A TRC converts an input of heat energy to light and electrical energy.

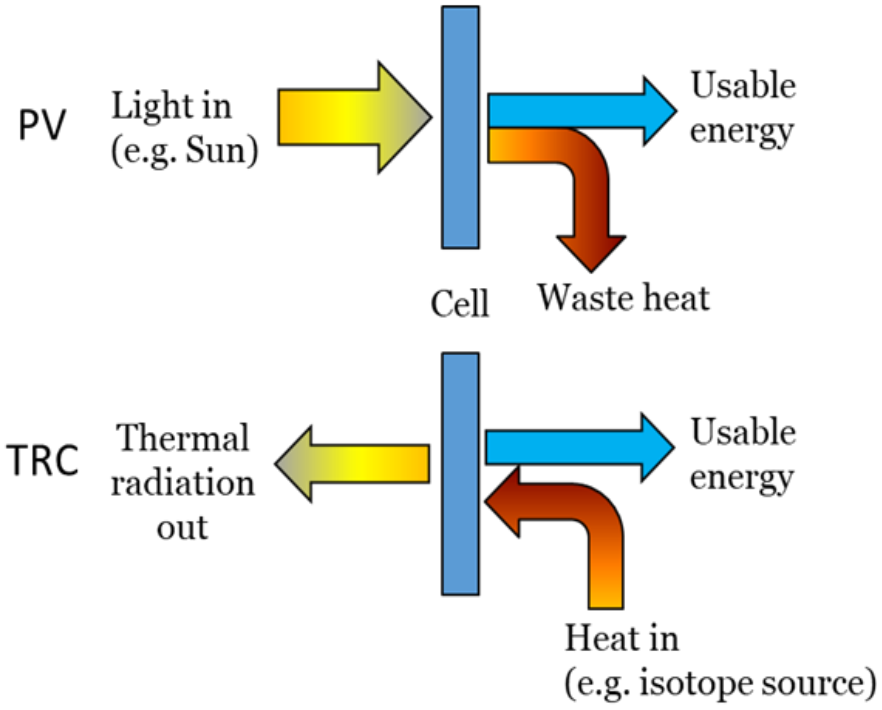

Figure 3 Diagram showing the heat and energy transfer between the environment and device for a photovoltaic cell and a thermoradiative cell

TRC operation can easily be understood when compared to the well-known PV cell. A PV cell is a p-n junction made from semiconductors such as silicon or gallium arsenide. When the device is viewing a body at the same temperature, nothing happens since there is no net flow of photons into the cell. When the PV device views a hot object such as the Sun, there is a large net flow of photons into the cell. This net flow causes excess carriers or electron-hole pairs to be

generated. The excess carriers can be swept out of the cell into an external circuit producing an electrical current [6].

A TRC works similarly. In this case, there is a net flow of photons out of the cell due to the cell being hotter than the ambient. Typically, this radiation would cool the cell until an equilibrium is met, but heat is continually supplied to the cell to hold its temperature constant. For a photon to be emitted, an electron and hole must meet and recombine. When this happens the distribution of electrons and holes are unbalanced and carriers from the external circuit are pulled in to fix this resulting in a photocurrent [2].

The ideal environment for TRC operation is exactly opposite that of a solar cell as well. The ambient temperature must be as cold and black as possible, and the cell must be as hot as possible. These conditions are readily available in space. Deep space provides an excellent cold, black environment and there are already heat sources commonly used for space missions such as an RTG. These are the main reasons why TRCs may be optimal for producing power in unlit parts of the solar system or beyond.

1.3 Blackbody Radiation

Blackbody theory was developed as a solution to “The Ultraviolet Catastrophe” which eventually led to the field of quantum mechanics and the widely used Planck Spectrum. An ideal blackbody absorbs all radiation incident on its surface and emits a unique spectrum dependent on its temperature alone which follows the equation below.

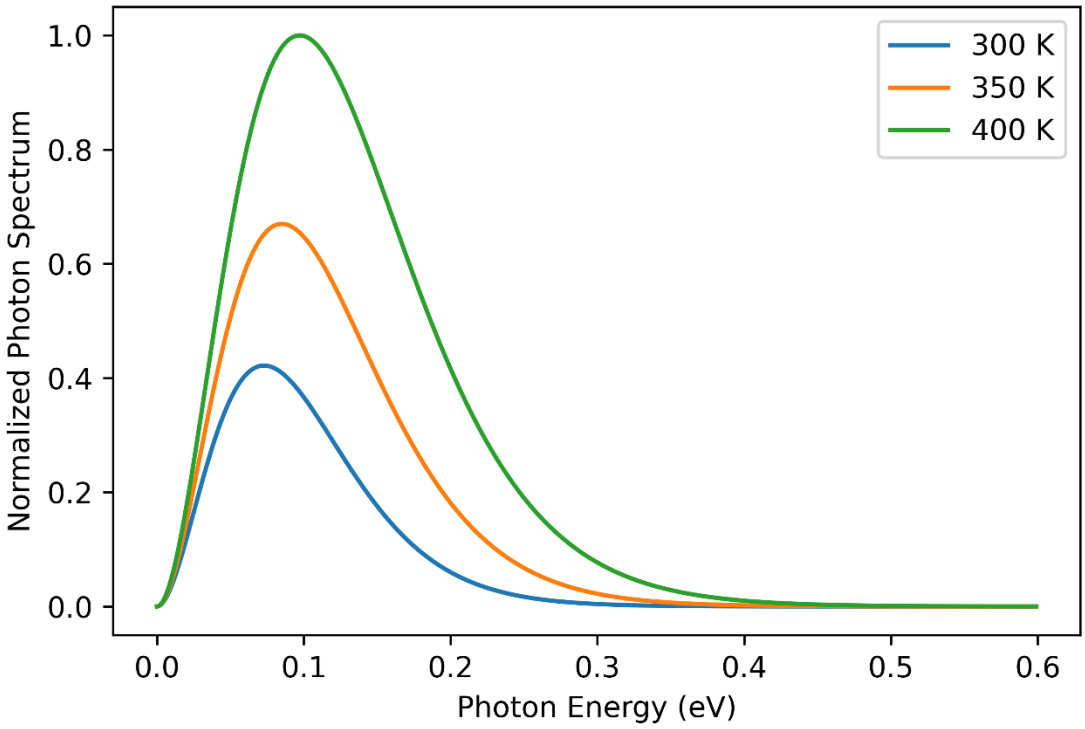

Figure 4 Compares the Planck spectrum for three different temperatures.

This spectrum defined in Equation 1 gives the energy radiated as light by an ideal blackbody for specific temperature and photon energy. Figure 4 shows the normalized blackbody spectrum for three different temperatures.

Equation 1

$$u(\epsilon) = \frac{8\pi}{(hc)^3} \frac{\epsilon^3}{e^{\epsilon/kT} - 1}$$

This can be integrated over a relevant photon energy range to obtain the total energy flux per unit volume in the determined range as shown in Equation 2.

Equation 2

$$U = \frac{8\pi}{(hc)^3}\int_{\epsilon_1}^{\epsilon_2}\frac{\epsilon^3}{e^{\epsilon/kT}-1}\,d\epsilon$$

To convert the integral above to a common table integral the substitution $x = {}^{\epsilon}/_{kT}$ can be used. Additionally, this can be converted from an energy flux to a photon flux which gives the number of photons emitted by a blackbody at each energy instead of the energy flux as shown in Equation 3.

Equation 3

$$N = \frac{8\pi}{(hc)^3}\int_{\epsilon_1}^{\epsilon_2}\frac{\epsilon^2}{e^{\epsilon/kT}-1}\,d\epsilon$$

If one desires the to know the total power or number of photons emitted by the cell, simply set $\epsilon_1 = 0$ & $\epsilon_2 = \infty$. This theory gives a allows us to understand the connection between heat and the emission of electromagnetic radiation in a quantifiable way that can be used to model a myriad of devices from incandescent lightbulbs to thermo-photovoltaics [7].

1.4 Detailed Balance

Detailed Balance is simply tracking the number of photons that flow through each possible path. As a result, this model can be simplified by reducing the possible photon pathways to only the most traversed. Of course, when some mechanisms are omitted, the accuracy will be reduced accordingly. It is important to carefully pick which mechanisms are included and omitted to ensure a major non-ideality is not overlooked. Figure 5 Diagram showing the main ways photons interact with the carriers in the semiconductor. shows the three main mechanisms

calculated in detailed balance. Thermalization occurs when a photon with energy larger than the bandgap is absorbed. This causes the electron to be excited to a high state and then rapidly decay to the bandedge releasing the difference as heat. Transmission occurs when the photon energy is lower than the bandgap causing the photon to pass through the material and not be absorbed. Emission occurs when an electron hole pair recombines emitting a photon. This reduces the number of excited carriers.

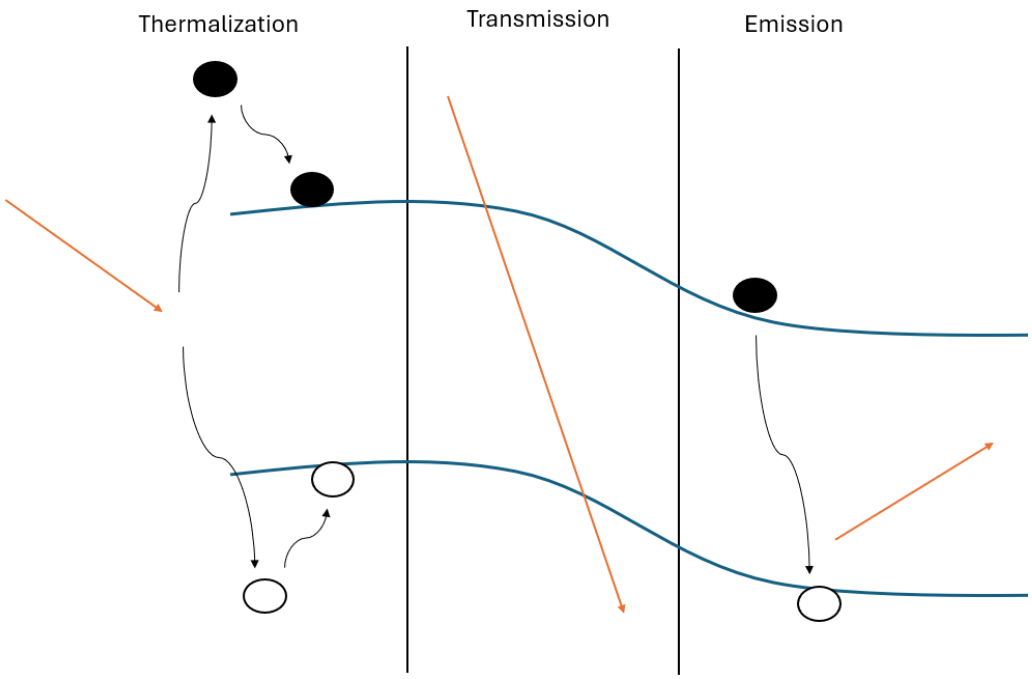

Figure 5 Diagram showing the main ways photons interact with the carriers in the semiconductor.

Detailed Balance was used to develop the famous Shockley-Queisser or Detailed Balance ultimate efficiency limit for a single p-n junction solar cell. Shockley and Queisser modeled the efficiency of a solar cell using the Planck distribution which assumed that the cell acts as a blackbody [8]. While this is generally a good assumption at equilibrium, a solar cell does not

operate at equilibrium since there is a required net photon flux into the cell. There exists a chemical potential that affects the carriers. De Vos and Pauwels introduced a modified Planck spectrum that accounts for this new potential [9]. This chemical potential can be modeled by adding a $\Delta\mu$ chemical potential term into the equation. While the concept of chemical potential is widely used and can be defined in many ways, for semiconductor p-n junctions the chemical potential is simply $\Delta\mu = qV$ which is the electron charge multiplied by the voltage across the junction.

Equation 4

$$\phi(\Delta\mu) = \frac{2\pi}{h^3c^2}\int_{\epsilon_1}^{\epsilon_2} \frac{\epsilon^2}{e^{(\epsilon-\Delta\mu)/kT} - 1}\, d\epsilon$$

Equation 4 gives the number of photons that are emitted from the body in the desired photon energy range $\epsilon_1 \; to \; \epsilon_2$. If one sets $\epsilon_1 = 0$ and $\epsilon_2 = \infty$ the integral will give the total number of photons emitted by the unit surface since all possible photo energies are within this range.

Notably, detailed balance assumes that only photons above the bandgap (E_g) are emitted or absorbed; any photons with energies below the bandgap incident on the surface are transmitted. Mathematically this means that $\epsilon_1 = E_g$ and $\epsilon_2 = \infty$ for both the cell and ambient calculations. This creates a range for the integrals that only counts photons with energies higher than E_g. In terms of material properties, this means that above the bandgap the emissivity of the cell equals one and zero below of course this is an idealization that will not occur in the real world, but the main purpose of detailed balance is not to directly predict device outputs but to put ultimate limits on things like efficiency and power output.

In the context of applying detailed balance, Equation 4 can be used to calculate the photon flux out of the cell, and Equation 3 is used to calculate the flux from any relevant body that does not have a chemical potential. In the case of a solar cell, this would be used to calculate the flux from the ambient surroundings and the Sun along with some geometric factors. The difference between the flux into and out of the cell determines the device properties. At equilibrium, the difference between these two values is zero meaning there is no net flow of photons into or out of the cell. When this difference is not zero, a net flow of photons exists, and carriers will be generated or removed accordingly. For a solar cell, there are more photons being absorbed than emitted due to the Sun. Under these conditions a solar cell will produce a negative current and a positive voltage as defined by typical diode directions.

While this is not a study on solar cells but TRCs, detailed balance and its techniques are still imperative. TRC applies the same methods of detailed balance and applies it to a new application. The only difference is the application of the equations. A TRC in space will not have a contribution from the Sun, and the surrounding temperature will be lower than the cell. These conditions result in a photon flux out of the cell, which is opposite that of a solar cell. Due to this inversion, many of the characteristics such as current and voltage are reversed in a TRC since the carriers are being pulled into the cell rather than being extracted out into an external circuit [2].

1.5 Organization

This thesis is organized into two main sections. First Chapter 2 will be a theoretical analysis of TRCs using detailed balance and other semiconductor equations. This includes some non-idealities such as Auger recombination, shunt, and series resistance losses as well as Shockley-Read Hall loss mechanisms. Secondly, Chapter 3 is an experimental portion where a

vacuum chamber and liquid nitrogen was used to recreate a space-like environment to test four different p-n junctions of 4 different bandgaps and two different materials. These results will then be compared to the theoretical calculations in the conclusive Chapter 4.

2 Theoretical Study of TRC Operation

2.1 The Ideal TRC

The ideal case may not be practically predictive of device characteristics, but it does give insight into the upper limits of possible power production and efficiency. Calculating detailed balance as described above with some approximations to simplify the math allows one to generate Current vs. Voltage (IV) Curves which will predict aspects such as Open Circuit Voltage (V_{oc}), Short Circuit Current Density (J_{sc}), maximum power production and maximum power point. These properties describe the performance of the device.

There are some common approximations that can be made surrounding the diode and detailed balance equations. First, Equation 4 can be simplified when the Boltzmann approximation holds which is true for bandgaps greater than $3kT$. In this case, a TRC can be modeled using the typical diode equation seen in Equation 5 [10].

Equation 5

$$J(\Delta\mu) = J_{0,rad}\left(e^{q\Delta\mu/kT} - 1\right) + J_{0,NR}\left(e^{q\Delta\mu/nkT} - 1\right) + J_{sc}$$

In Equation 5, there are a few new quantities. First, $J_{0,rad}$ and $J_{0,NR}$ which are the radiative and non-radiative recombination currents respectively. $J_{0,rad}$ is the amount the cell radiatively recombines given by the form $q\phi(0)$. $J_{0,NR}$ is the current that flows through non-radiative recombination mechanisms. For the ideal case this value is null but is important when assessing the quality of actual devices. Secondly, there is the ideality factor n which helps describe the nature of the non-radiative recombination but is not important in this section.

Finally, J_{sc} is the short circuit current mentioned above. This is the current that flows when the potential is zero given by Equation 6 where ϕ_c represents the photon flux out of the cell and ϕ_a is the photon flux from the ambient into the cell. Figure 6 Diagram showing the emission and absorption of photons. In this case there are more photons being emitted than are absorbed.shows a diagram of the flux difference for a TRC, more photons are emitted than absorbed.

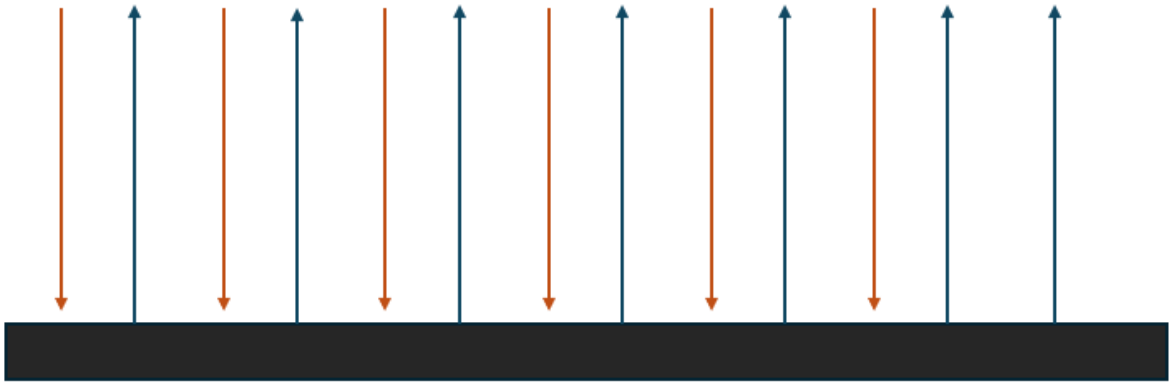

Figure 6 Diagram showing the emission and absorption of photons. In this case there are more photons being emitted than are absorbed.

The quantities given for J_{sc} and $J_{0,rad}$ can be used to manipulate Equation 5 which results in a function that can be used to directly calculate the current through an ideal TRC given by Equation 7 [10].

Equation 6

$$J_{sc} = q(\phi_c(0) - \phi_a)$$

Equation 7

$$J(\Delta\mu) = q[\phi_c(0)e^{q\Delta\mu/kT} - \phi_a]$$

Figure 7 shows the current vs. voltage curves generated using Equation 7 for an ideal TRC (solid purple) and photovoltaic (dash-dot teal) to compare their operation. Figure 7 also

includes the IV curve of a diode at equilibrium (dashed blue). The temperatures difference for both the TRC and photovoltaic case is 700 K. As seen in Figure 7, a thermophotovoltaic has a positive voltage with a negative photocurrent, and a TRC has a positive current with a negative voltage.

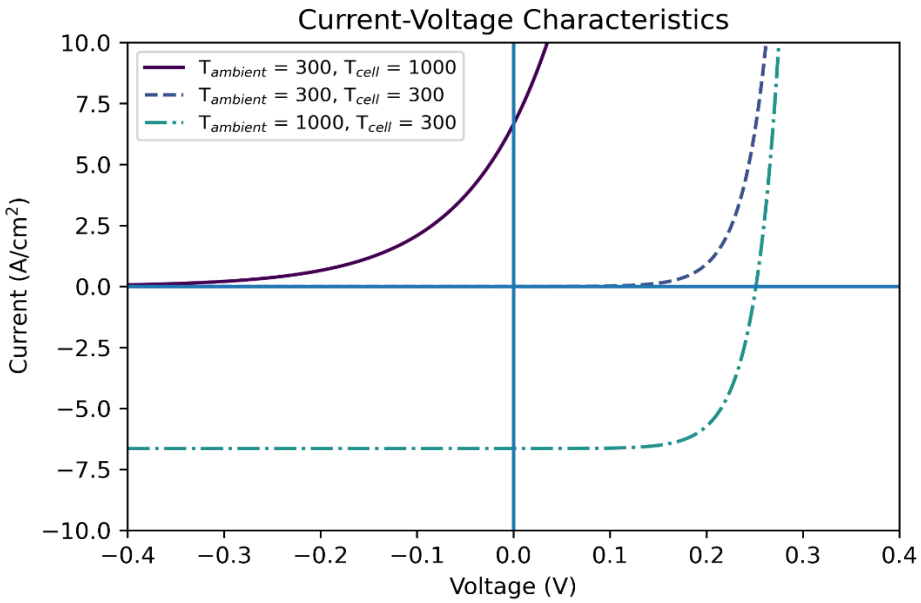

Figure 7 Compares the ideal IV curves of a TRC (solid purple), a diode at equilibrium (dashed blue) and a thermophotovoltaic (dash-dot teal) which is a solar cell with a spectrum from a hot body that isn't the Sun.

Power can be found by multiplying the current and voltage. As shown in Figure 8, the potential power generation of a TRC does not match the potential of photovoltaics for the same temperature difference. Despite this, there are many potential scenarios where TRCs may perform better than photovoltaics despite this difference in raw power potential.

Since the integral calculated to find ϕ_c is dependent on the bandgap as well as the temperature of the emitting body, in this case the cell, the current and power production are also highly dependent on these inputs as well. Lowering the bandgap means more carriers are

thermally excited into the conduction band which allows for greater radiative recombination which increases power production. The same logic applies to raising the temperature of the cell.

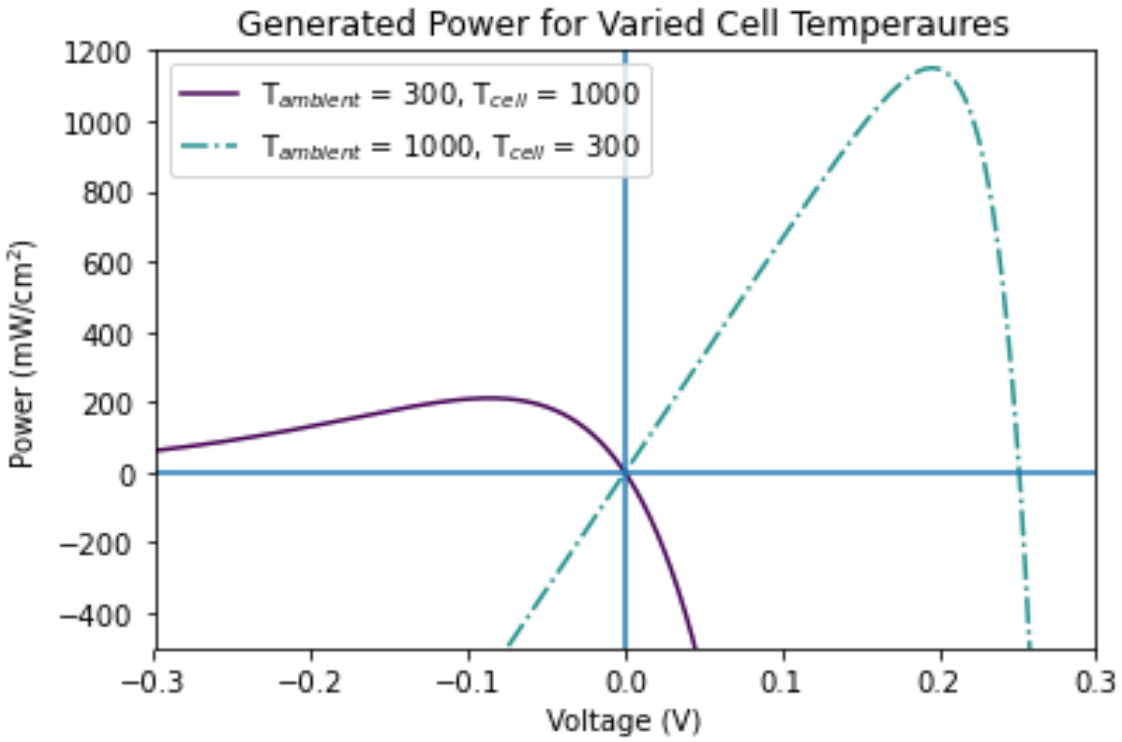

Figure 8 Power production of ideal TRC (solid purple) and ideal thermophotovoltaic (dash-dot teal)

Since there are two important independent factors, it is useful to create a map of the ideal case TRC in the form of a contour plot found Figure 9. In the ideal case, a TRC with the lowest bandgap at the highest temperature will perform the best. The next section will discuss a non-radiative mechanism that will alter this conclusion.

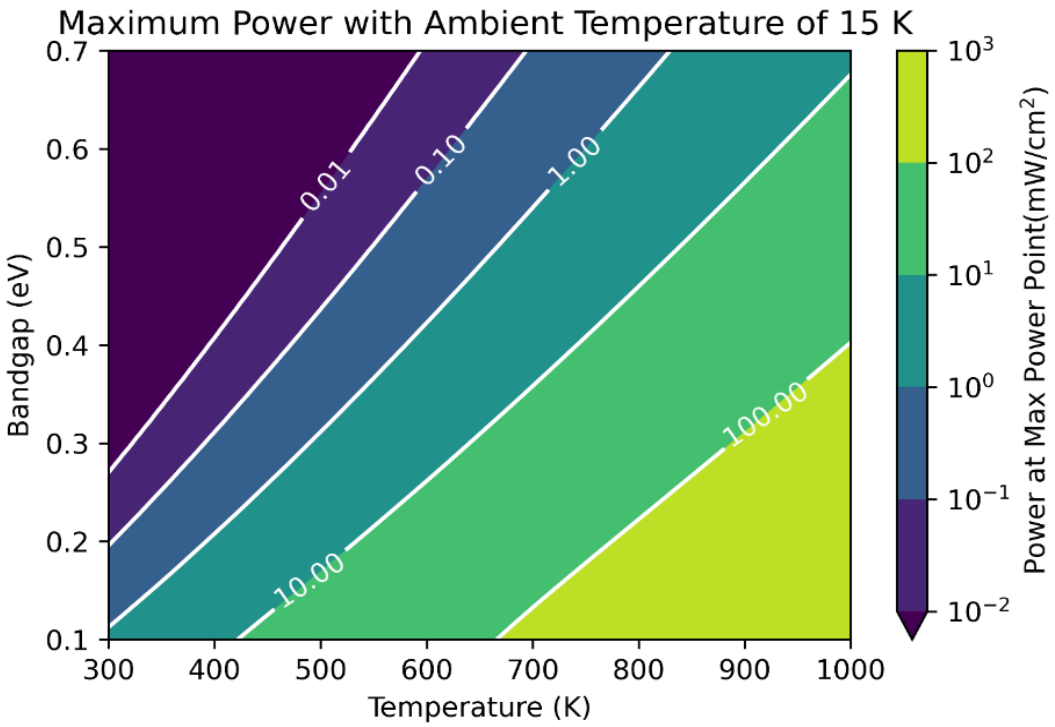

Figure 9 Contour plot showing power generation at the maximum power point for many different bandgap and cell temperatures combinations. The ambient temperature used to generate this plot was 15 K to model a space-like ambient.

Power generation isn't the only consideration when discussing a new power generating device. Efficiency is also an important factor to consider. Efficiency is defined as $\frac{P_{out}}{P_{in}}$ or the ratio between the input power and returned usable electrical power. In a TRC the input power is the heat supplied to hold the cell temperature above the ambient. In a solar cell the input power is the power from the Sun. This can be quantified for a TRC in Equation 8 [2].

Equation 8

$$\eta = \frac{P_{out}}{P_{heat}} = \frac{P_{out}}{P_{out} + E_r - E_a}$$

The energy supplied to maintain the device temperature, shown as P_{heat} can be defined as the difference between the power extracted as electrical power, P_{out} plus E_r is the energy

radiated from the cell, minus E_a, energy radiated into the cell from the ambient. These values can be calculated using Equation 2 with the same chemical potential modification as done for photon flux. For the ambient, the chemical potential is simply zero. This definition stems from the

The efficiency at each voltage for a few different bandgaps is found in Figure 10 . The efficiency for a TRC approaches very high efficiencies as voltage increases, but as shown in Figure 8 the power generated at these high voltages is extremely low compared to the power generated at the maximum power point.

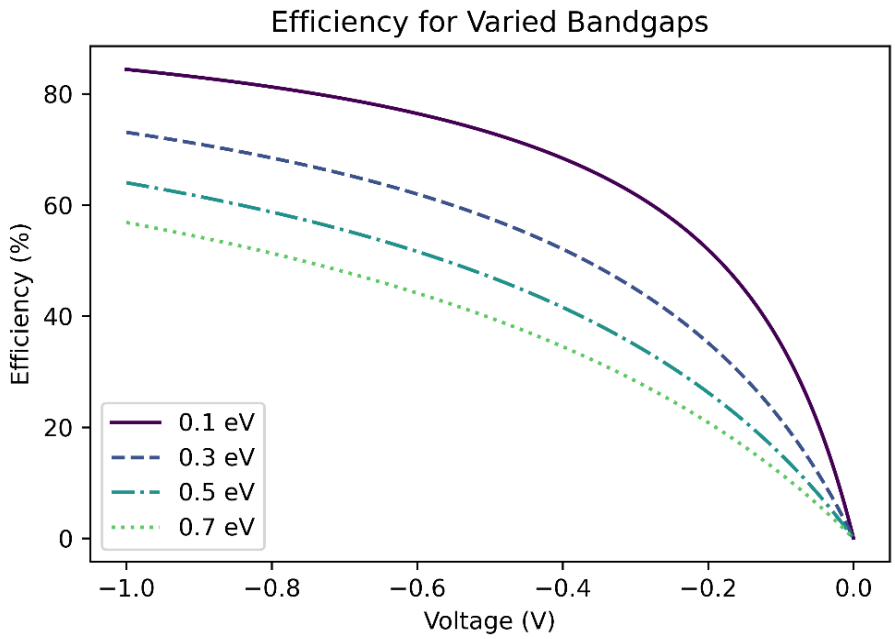

Figure 10 Shows how efficiency changes as voltage changes for the ideal TRC for a few different bandgap energies.

This is one major difference between a TRC and a photovoltaic cell. The TRCs maximum power point and maximum efficiency point are not at the same voltage as they are in photovoltaics since E_r is in the denominator of Equation 8 and is dependent on voltage. The input for photovoltaics is the Sun and is not dependent on voltage in any way. TRC efficiency

does not rise indefinitely, eventually, the voltage will reach the V_{oc} and efficiency will drop to zero since no power is being produced.

Now, one can put an upper limit on possible power production when used at RTG temperatures with deep space as the ambient by considering the ideal case. The hot-side temperature of the thermoelectrics is approximately 815 K [11]. If a TRC were to replace the current thermoelectric devices, their temperature would match that of the hot-side and produce a maximum power of 57.3 mW/cm^2 with a short circuit current density of 2.2 A/cm^2. The shell of the MMRTG has a surface area of approximately 4150 cm^2. If this entire surface could be used for TRC power generation at the hot-side temperature, the ideal system would produce almost 240 W of usable electrical power. The current MMRTG design produces 110 W of electrical power using the mentioned thermoelectric devices [1]. This corresponds to a power density of only 26.6 mW/cm^2 which is about half of the theoretical TRC power density.

In the case where a TRC is used in tandem with the current thermoelectrics, the TRC cell temperature would match the outer shell or fin-root temperature. This is the temperature of the radiating fins near the main body of the MMRTG. This region has a temperature of 485 K [11]. The ideal TRC at this temperature produces 0.92 mW/cm^2 and a short circuit current density of 59.9 mA/cm^2. If the same calculation is done as above, the TRC at this temperature would only produce 3.75 W. Adding this to the current electrical power production from the thermoelectric devices gives a total power production of 113.75 W. In the ideal case, the TRC can outperform the current system.

Of course, there are other considerations than just pure detailed balance calculations. The solar system has many radiating bodies that can increase the flux of photons into the cell, in turn reducing the overall current and power generation. For example, if a satellite equipped with

TRCs rotates to view a planet or the Sun, more photons will be absorbed by the cell than if it only views deep space. Space photovoltaics has a similar issue when the cells rotate out of view of the Sun, typically this issue can be resolved by storing extra electrical power in batteries. Secondly, there are non-radiative recombination mechanisms that will reduce efficiency as well. This includes mainly Shockley-Read Hall recombination, and Auger recombination but there are others as well.

2.2 Auger Recombination in a TRC

Auger recombination is a three-body recombination mechanism that is extremely relevant in low bandgap or high temperature devices. Essentially, an excited electron recombines with a hole, but instead of producing a photon, a second electron is excited to a higher state. This second electron will decay back to the band edge releasing the extra energy as heat or phonons. The energy stored in the first excited electron is lost to heat. A diagram of this process can be found in Figure 11. III-V photovoltaics typically ignore this mechanism since their bandgaps are higher which reduces the rate of Auger recombination to almost zero. Despite this, III-V photovoltaics do need to account for Auger recombination at high carrier concentrations. Auger recombination is a major limiting factor in silicon photovoltaics. Additionally, Auger is a limiting factor for other devices as well such as Light Emitting Diodes (LEDs) when operated at high current densities. In short, Auger recombination is a major efficiency consideration when the carrier concentration is increased beyond a certain level. Raising the device temperature or reducing the bandgap both raise the carrier concentration. A TRC device has a low bandgap and is operated at a high temperature meaning that Auger recombination will be a limiting factor for the efficiencies of TRCs [12].

Most of the work studying Auger recombination comes from the infrared detector field. These detectors need to have low bandgaps since they detect photons in the infrared region which lies between 780 nm and 1 mm. Photons in this wavelength range have an energy between 1.59 eV and 0.00124 eV. If the detector aims to capture most of the infrared light, a low bandgap energy device is required otherwise most of the light will transmit through the device and not be absorbed. These devices can have bandgaps as low as 0.1 eV.

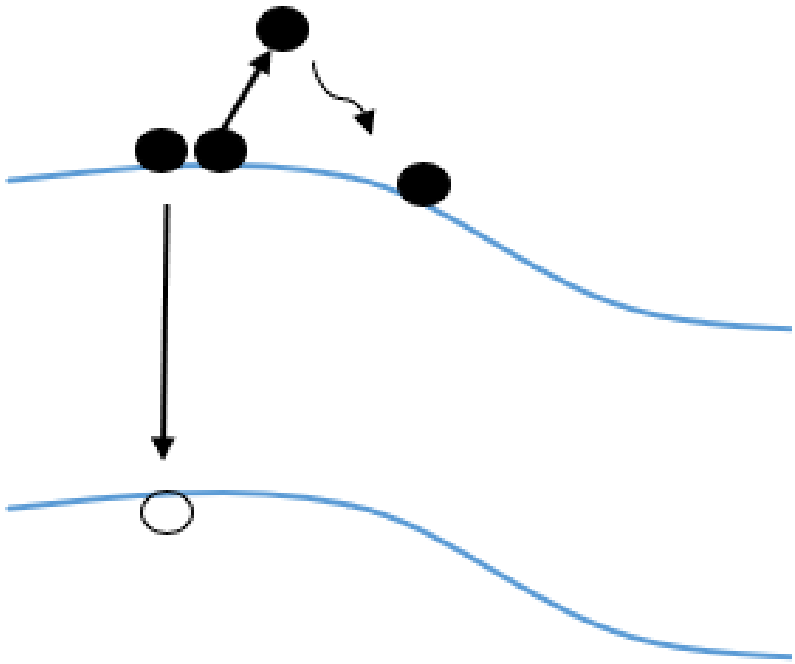

Figure 11 Diagram of Auger recombination. An excited electron hole pair recombine, and the energy is transferred to a second excited electron. This extra energy raises the second electron's energy above the band edge. The second electron then rapidly decays back to the band edge, and the energy is released as heat and is considered to be lost.

There is a way to model the recombination within p-n junctions which is found in Equation 9 [13]. This equation models the three main types of recombination found in these types of devices and applies to TRCs. U is the total recombination rate in the device. n is the carrier density which can be calculated using material properties such as the Auger recombination coefficient, electron and hole effective masses, device temperature, and bandgap [14].

Equation 9

$$U = An + Bn^2 + Cn^3$$

Each term gives the recombination rate of one type of mechanism. An is the single carrier term and incorporates defect recombination such as Shockley-Read Hall. This type of recombination is strongly dependent on material quality and will be omitted for this section. Bn^2 is the two-body recombination term and involves radiative recombination. Cn^3 is the three-body recombination term and involves all types of Auger recombination. The coefficients in these terms are material properties and fitting parameters. C is the Auger Coefficient and a value of Indium Arsenide was used [15]. To calculate the reduction in current density due to Auger recombination, insert a radiative efficiency term that follows $\frac{B}{B+Cn}$ [13]. This term will always be less than or equal to 1 and will reduce the overall current density by the radiative efficiency loss due to Auger recombination.

Equation 10

$$J(\Delta\mu) = \frac{B}{B + Cn} q[\phi_c(0)e^{q\Delta\mu/kT} - \phi_a]$$

Equation 11

$$n = 2\left(\frac{2\pi kT}{h^2}\right)^{\frac{3}{2}} (m_n m_p)^{\frac{3}{4}} e^{-\frac{E_g}{2kT}}$$

Equation 11 can be used to calculate the intrinsic carrier concentration [16]. This can then be used to calculate the Auger recombination rate and Auger adjusted current density. m_n is the electron effective mass and m_p is the hole effective mass, which are material properties. This involves an empirical formula that depends on the composition of the material [15]. For this study, the formula for InAsSb and the composition was set such that the bandgap energy would

be 0.3 eV. This band gap closely matches the a composition of InAsSb that is lattice matched to an InP substrate. Also, the Auger Coefficient used was $2.2 \times 10^{-27}\ cm^3/s$.

Carrier concentration is dependent on both the bandgap and temperature of the cell. Despite this, the concentration is exponentially dependent on bandgap but only dependent on the $^3/_2$ power of temperature. This means that a change in bandgap will have a more profound effect on the carrier concentration (and in turn Auger recombination rate) than a change in temperature will.

The introduction of Auger recombination into this model has some interesting effects. First, at low enough temperatures, the carrier concentration reduces such that the effect of Auger recombination is limited as shown in Figure 12. At low temperatures, the difference between the ideal and Auger incorporated power generation is minimal. At high temperatures, each degree begins to have a smaller increase in power production since Auger recombination is strong in this region. A balance must be struck such that Auger recombination is not too strong, but also that the temperature is sufficiently high enough to produce a usable amount of power.

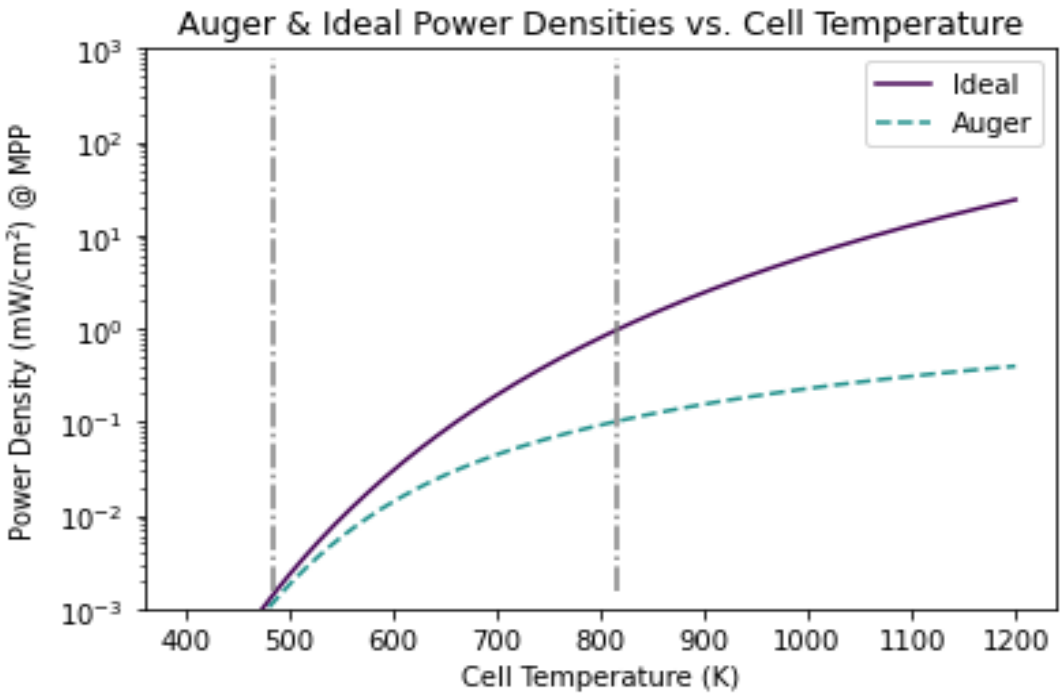

Figure 12 Compares the power generation of an 0.3 eV ideal TRC and when Auger recombination is included. The grey lines represent the two possible operating temperatures of 485 K and 815 K.

Material Property	Value
Radiative Recombination Coefficient (B)	$1.1 \times 10^{-11}\, cm^3/s$
Auger Recombination Coefficient (C)	$2.2 \times 10^{-27}\, cm^6/s$
SRH Recombination Coefficient (A)	$0\ \ 1/s$
Hole Effective Mass (m_n)	$0.401 m_0$
Electron Effective Mass (m_p)	$0.0197 m_0$

Table 1 Table of material properties used for Auger section of this thesis.

Another aspect of the device that affects the Auger recombination is the bandgap of the cell. Figure 13 shows that lowering the band gap dramatically increases the effects of Auger recombination and reduces the power as a result. As the bandgap is increased, the Auger effects diminish until they are negligible. This is why Auger recombination is typically not considered in III-V photovoltaics. Their bandgaps are beyond the threshold such that this recombination mechanism is rare. Since a TRC will produce more power at lower bandgaps, Auger recombination is a very important mechanism to consider.

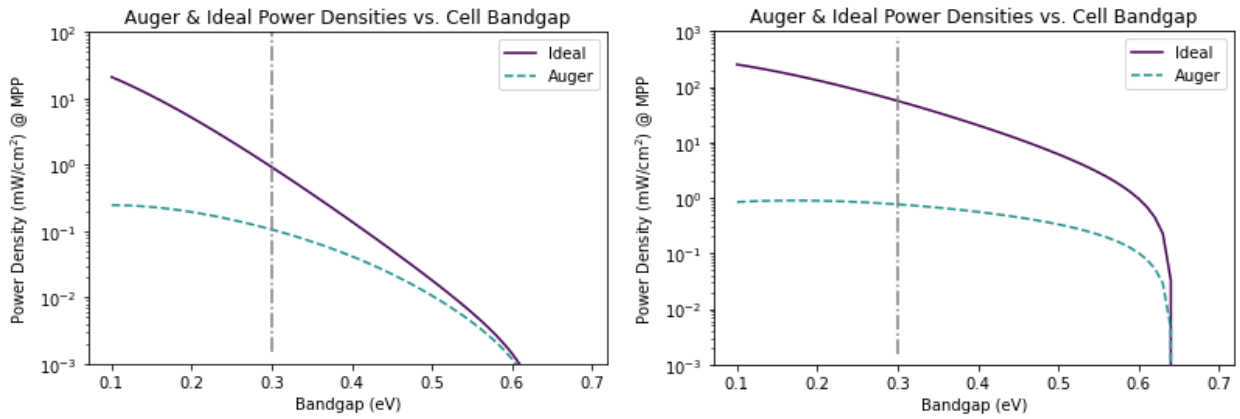

Figure 13 Shows the difference between power generation for the ideal and Auger case for the two operating temperatures. Left) 485 K Right) 815 K. The grey line marks the 0.3 eV bandgap which is of interest as it is near many possible material bandgaps.

Like Figure 9 for the ideal case, it is enlightening to combine the effects of the two independent variables into one plot which is done for Auger considerations in Figure 14. Unlike the ideal case, it is no longer always beneficial to reduce the bandgap. If the bandgap is too low, the device will be Auger limited and reducing the bandgap will begin to reduce the power output. The same goes for temperature. If the bandgap is not sufficiently low, an increase in temperature will not meaningfully increase the power output. The optimal bandgap according to this

calculation appears at 0.2 eV where a further reduction in bandgap will begin to diminish the total power output, but an increase in temperature will still produce additional power.

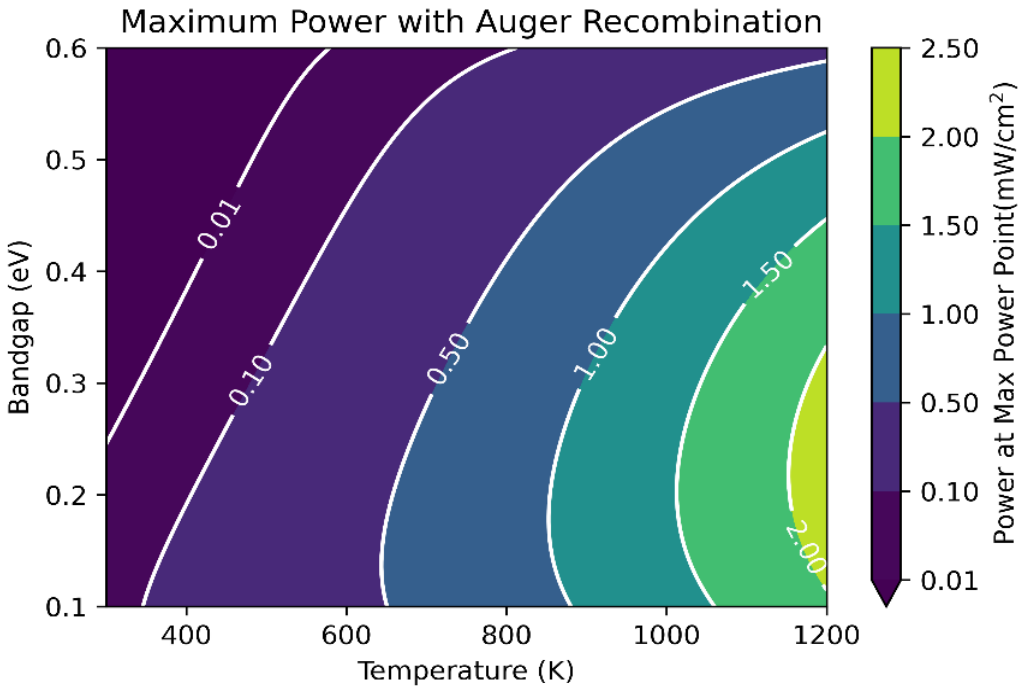

Figure 14 Contour plot of power generation at the maximum power point for a TRC including Auger recombination.

2.3 Other Non-Idealities

There are many different sources of efficiency loss that can be included in a model. The two most common are Shockley-Read Hall (SRH) and resistance losses. SRH recombination is associated with material quality and the number of trap states within the device. This can vary widely depending on stress, strain, interface quality and overall material uniformity. To calculate the SRH recombination rate, use the general form of carrier lifetime that relates lifetimes to recombination rates as shown in Equation 12. n is the carrier concentration and τ is the lifetime which depends on the material properties but was found to be $5 \times 10^{-7}\ S$ for InAs [17]. Now we

can use the “ABC” model above and keep the first SRH term. This gives a new radiative efficiency term that is $\frac{B}{\frac{A}{n}+B+Cn}$. Like in Equation 10, this radiative efficiency term is multiplied by the total current given by pure detailed balance. This will reduce the current by an amount relative to the strength of each type of recombination.

Equation 12

$$R_{SRH} = \frac{n}{\tau_{SRH}}$$

Additionally, devices have series and shunt resistances. Series resistance is a typical resistance in series with the load or device that will reduce the current and power. A perfect circuit has zero series resistance. Shunt resistance is a resistance in parallel with the load or device and acts as a passage for current to “leak” out of the circuit which also presents a loss. Ideally, this resistance is infinite to reduce the amount of leakage to zero. A circuit diagram depicting these elements is found in Figure 15 Circuit diagram for a thermoradiative cell. Includes a non-radiative diode as well as shunt and series resistance losses..

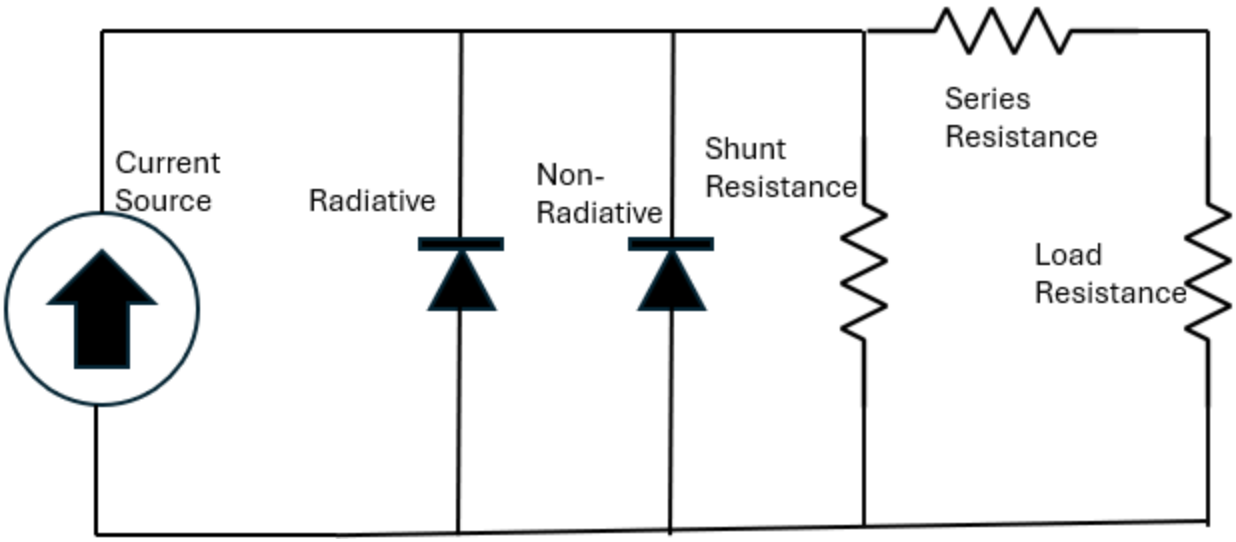

Figure 15 Circuit diagram for a thermoradiative cell. Includes a non-radiative diode as well as shunt and series resistance losses.

Equation 13

$$J(V) = \frac{B}{\frac{A}{n} + B + Cn}\left(J_{0,rad}\left(e^{\frac{-q(V+JR_S)}{kT}} - 1\right) + J_{0,nr}\left(e^{\frac{-q(V+JR_S)}{nkT}} - 1\right) + J_{sc} - \frac{V + JR_s}{R_{sh}}\right)$$

Equation 13 gives the current density when considering non-radiative recombination as well as series and shunt resistances [10]. The non-radiative term in this study has been ignored since the non-radiative recombination's are calculated with a different method, the radiative efficiency term. Equation 13 cannot be solved analytically except for the case of zero series resistance. Otherwise, this must be solved computationally. It may look like Equation 13 does not depend on the photon flux from the cell or ambient, but recall Equation 6 for J_{sc}. This calculation was done for the ideal, series and shunt resistance cases found in Figure 16 for a series resistance of 20 $m\Omega cm^2$ and a shunt resistance of 200 $m\Omega cm^2$. When calculating for the series resistance loss, the shunt resistance was set very high at 1000 Ωcm^2 and to show the shunt loss the series resistance was 0 $m\Omega cm^2$.

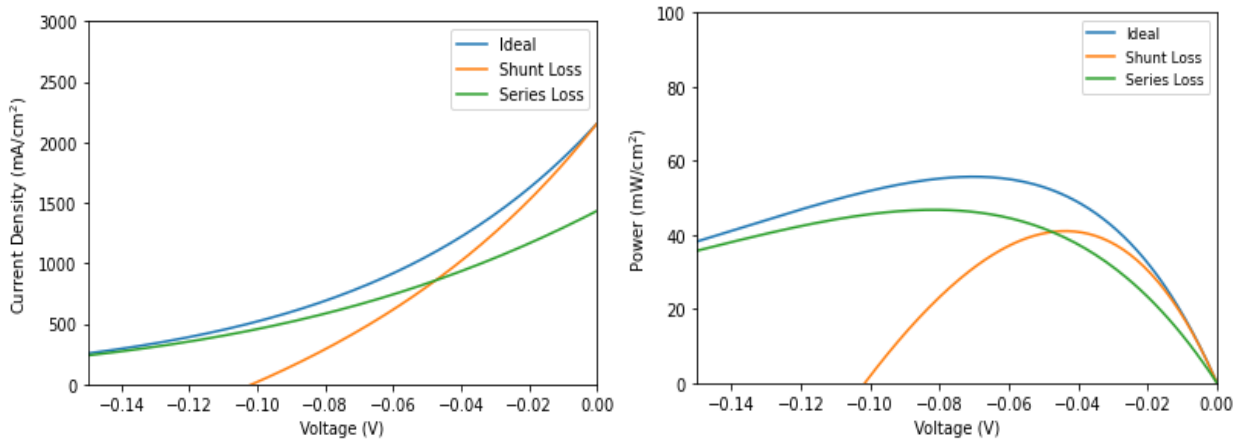

Figure 16 Current and power plots showing the effects of series and shunt resistances. These show the effect of each resistance individually, but they can be combined in the presence of both types of resistances.

Both types of resistance affect the devices differently. Series resistance reduces the current through the device which affects the short circuit current massively but does not affect the open circuit voltage. Shunt resistance decreases the open circuit voltage but does not reduce the short circuit current. Both loss types will decrease the overall power production albeit in different ways. Real devices have a combination of both series and shunt resistance losses that reduce overall device performance.

All these loss mechanisms that have been modeled can be combined to give a full picture of how a real device will perform. This will require some material constants that can be found in the literature, as well as some individual device specifications. In later sections this full model will be compared to experimental data.

3 Experimental Testing of Diodes as TRC

As discussed in the previous chapter, a TRC will produce power when the cell temperature is higher than the ambient temperature. This temperature difference will cause the emission rate of photons from the cell to be higher than the absorption rate from the ambient. This will produce a current proportional to that difference in photon flux.

Controlling the temperatures of the ambient and the cell provided an experimental challenge. The major temperature fluctuations made holding vacuum a challenge as well. Despite this, an experimental setup was built, and devices were able to be tested under space-like conditions. This setup utilized a modified Janis cryostat which provided a vacuum chamber, electrical connections, and a stage heater. Figure 17 shows a cross-sectional diagram of the chamber.

3.1 Janis Cryostat System

The Janis Cryostat provided an almost perfect solution to many of the issues surrounding this test. An overhead image of this system can be found in Figure 18. It includes a four-point electrical probes setup which eliminates the resistance loss through the arms by using two different probe sets to source the voltage and measure the current. The device stage is also electrically connected which makes contacting devices with a back-contact easier. This system uses dual-axial cables which reduce cable loss and environmental effects. These probe arms also make the electrical connection between the device inside the main vacuum chamber to the outside. The stage and all its components are housed in a vacuum chamber.

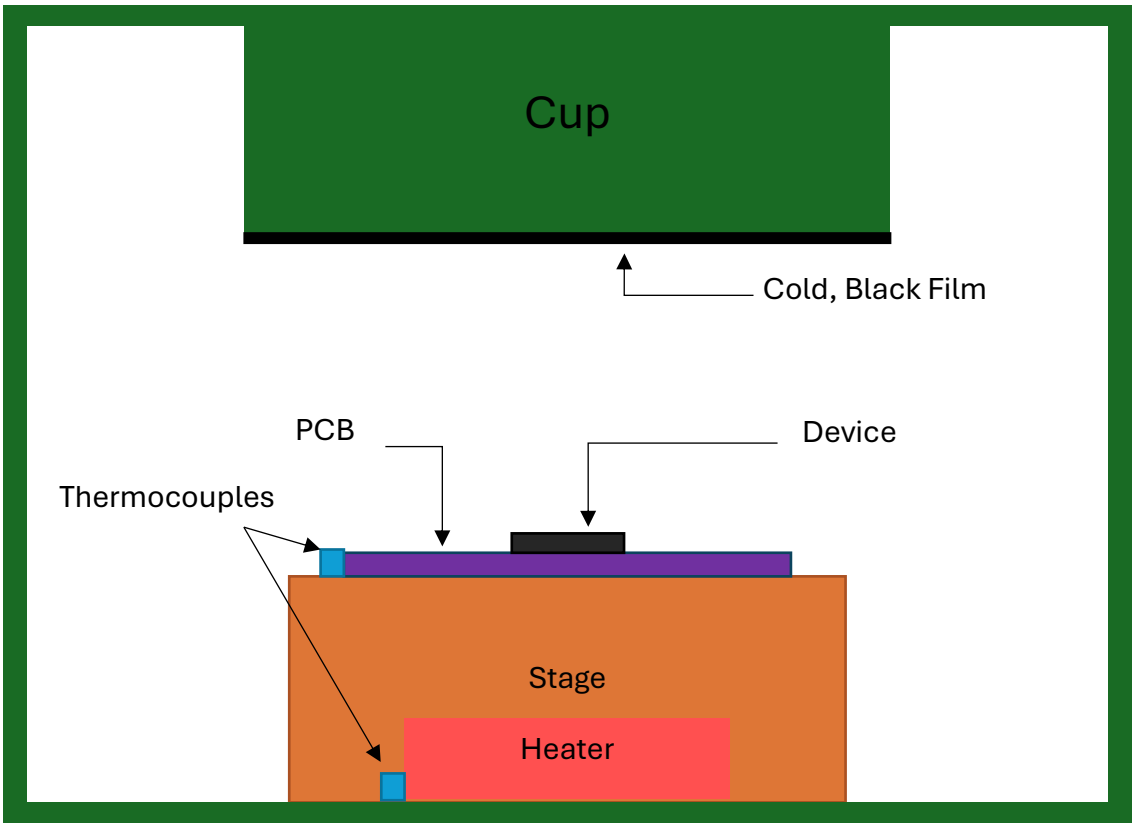

Figure 17 Diagram of the cross section of the Janis vacuum chamber during a test.

The system uses Lakeshore 330 Temperature Controller to manage the stage temperature. The stage can be held within a temperature range between 80 K and 500 K. It has piping that

allows for the flow of liquid nitrogen which cools the stage, and a heater to warm it up. The temperature controller uses the heater to counteract the cooling and keep the temperature stable using a Proportional, Integral, Derivative (PID) technique. This is a very common system that will precisely target a designated setpoint and maintain it continuously.

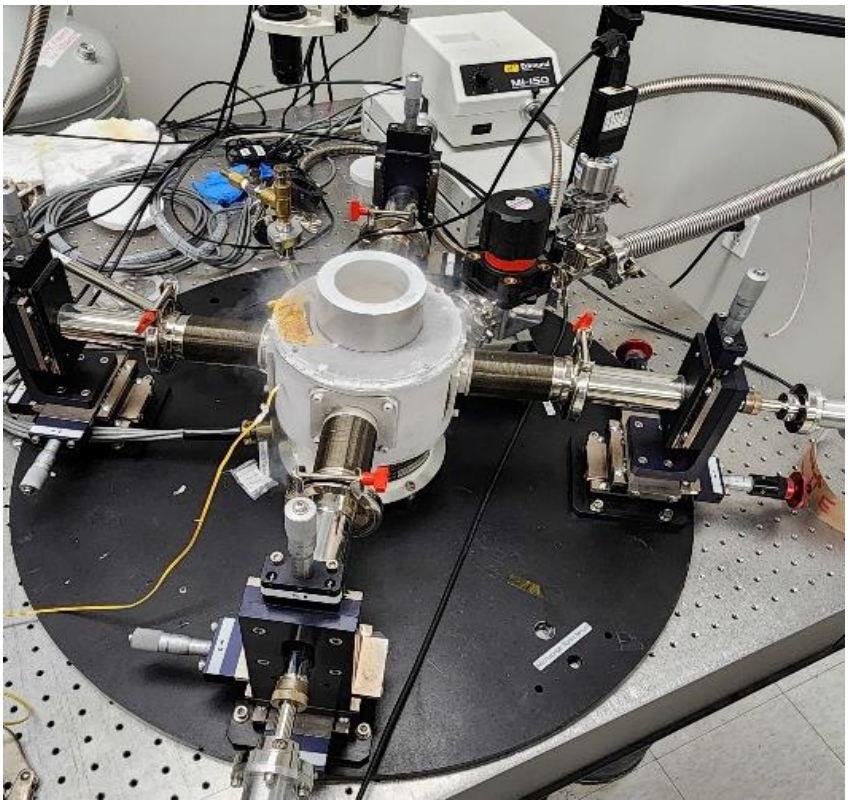

Figure 18 TRC experimental setup which shows the Janis Cryostat and its four electrical probe arms. The Lakeshore temperature controller can be seen in the upper right.

The Lakeshore uses measurements from the internal thermocouples on the stage and near the heater to inform its PID response. Figure 19 shows the temperatures of both thermocouples as measured by the Lakeshore. The temperature of the stage and heater are different, but both are steady until a setpoint change is made.

The Lakeshore 330 Temperature Controller also uses a GPIB interface so it can be controlled with Python on an external laptop. This made syncing the stage temperature movements and the current-voltage data collection seamless.

To source the voltage necessary to measure the current-voltage curves, a Keithley 2400 Sourcemeter was used. This allowed for voltage to be sourced with microvolt sensitivity while simultaneously measuring the current through the device. This device is equipped with a GPIB

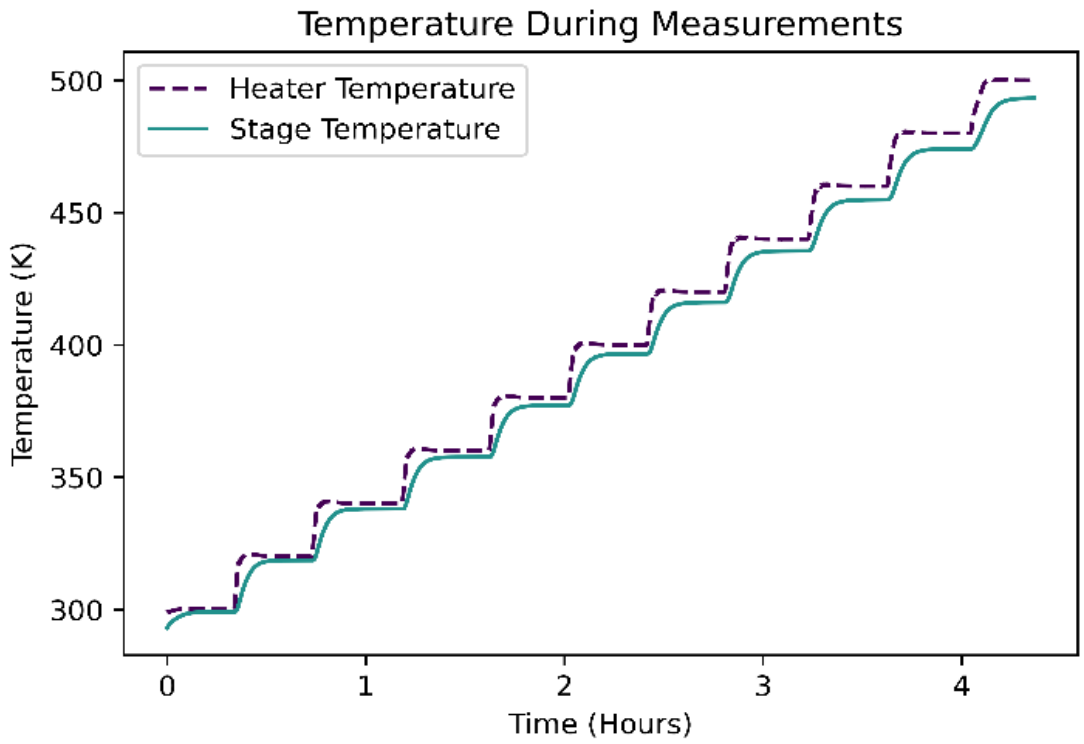

Figure 19 Shows the measured temperatures of the two thermocouples in the stage. This shows that the PID controller works properly and can hold a steady temperature until the setpoint is changed.

cable connection that allows it to be controlled using Python on an external laptop. This made the measurement automatic and very fast compared to manually changing the voltage at each step. This capability allowed for many more data points to be collected, which increased the resolution and range of the data collection.

3.2 Lid Design and Fabrication

The cell temperature can be controlled by the stage inside the Janis, but the ambient cannot. For this experiment to accurately model a spacelike environment, the device will need to view a very low emitting surface. Blackbody theory tells us that a very cold body will emit few photons. Typically, the Janis cannot provide a cold environment, only cool the cell down so a custom lid for the vacuum chamber was fabricated.

This new lid fits the vacuum chamber but has a cup in the center that can be filled with liquid nitrogen which cools it down. This lid was designed with Autodesk Inventor and fabricated in the RIT machine shop. It consists of two pieces, a flange, and a cup. The design view for these three pieces can be found in Figure 20. The flange was water jetted out of an aluminum plate with an inner diameter of 81.3 mm and an outer radius of 167.9 mm. It also has four through holes so it can be secured onto the Janis chamber and create the seal.

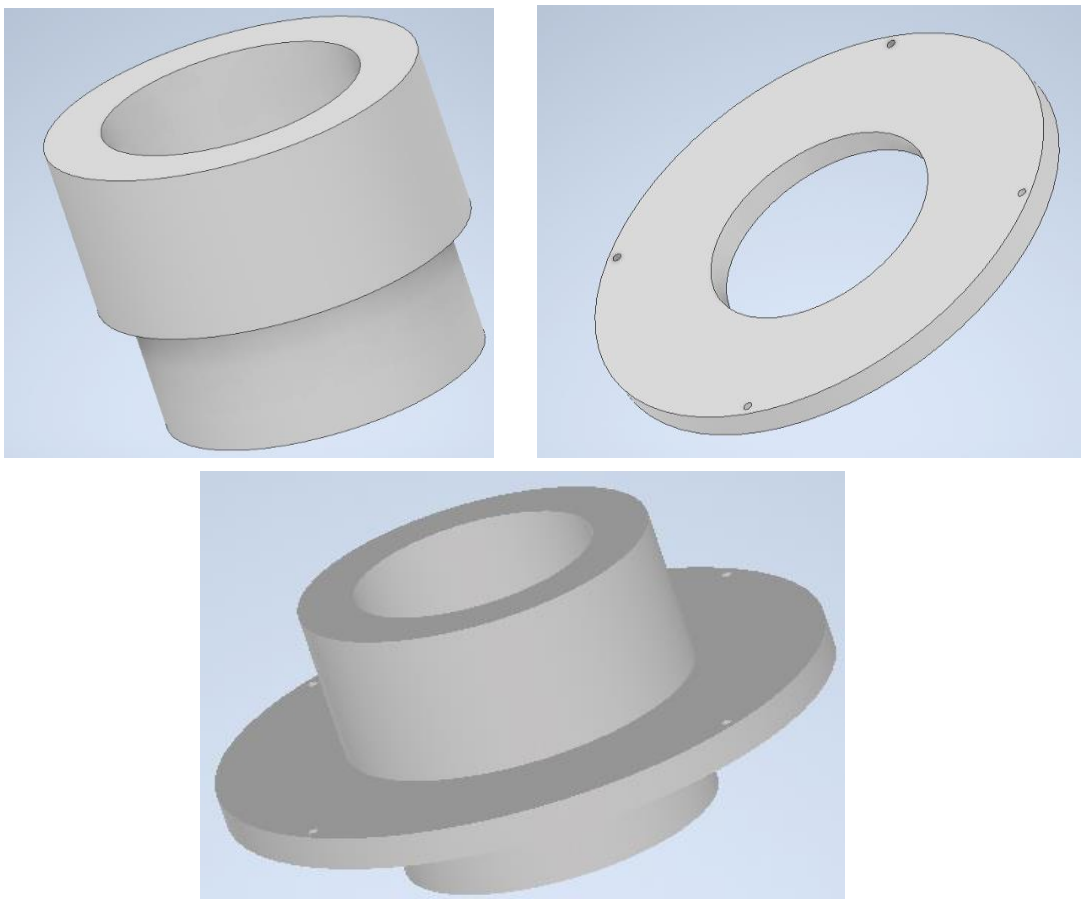

Figure 20 CAD design of the lid parts and assembly. Upper Left) Cup to hold liquid nitrogen Upper Right) Flange with screw holes to match vacuum chamber Bottom) Assembly of the two parts.

The cup was made on a lathe from an aluminum round. The top has an outer diameter of 95.25 mm, and the bottom has a diameter of 81.3 mm. The top and bottom need different diameters so the lid can fit into the chamber properly while maximizing the amount of liquid it can hold. The inner diameter is uniform at 66 mm. In total the cup can hold 261 mL. A lip was cut into the cup for the flange to seat into during welding. The cup and the flange and cup were welded together creating the final part shown in Figure 21.

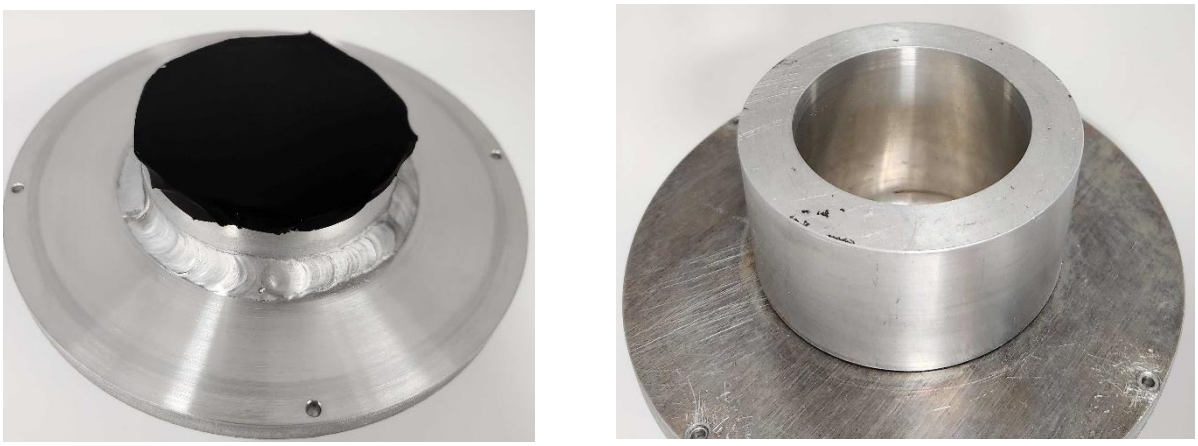

Figure 21 Finished lid with cup, flange, and film. Left) Underside of lid that is inside the chamber during operation. Right) Top side of lid with cup opening to be filled with liquid nitrogen.

Finally, a black metal velvet film manufactured by Acktar was applied to the viewing surface. This is an ultra-black low emission film that reduces the emission dramatically. This film is fragile and was replaced periodically due to damage.

During the experiments, this lid is cooled by continuously filling the cup with liquid nitrogen. The lid would cool to 95 K repeatably in thirty minutes. This temperature was measured on the top side in the corner made by the cup and flange. Due to aluminum's high thermal conductivity, it is assumed that the underside of the lid is at or below this temperature as well.

This lid allowed for the device in the chamber to view a very cold and black surface, which reduces the ambient flux into the cell and mimics what a cell in space would see. While the lid was ultimately successful, it did provide some challenges. Due to the extreme temperature cycling the original Nitrile O-ring that creates the vacuum seal would harden and lose its ability to fully seal. This would result in a loss of vacuum sometime during the lid cooling process. To combat this, a low temperature Teflon O-ring replaces the stock O-ring. This new O-ring could withstand the cooling process and would lose minimal vacuum during the experiment.

3.3 Printed Circuit Board

Typically, the Janis probes arms make electrical connections to devices with metal contacts either on the top, bottom, or both. The connection is made by placing tiny metal tips onto these contact pads. This would not work for this experiment for a couple of reasons. First, the devices used do not have these contact pads since they are bought off the shelf and not fabricated in house, Secondly, due to the extreme temperature fluctuations the probe arms would move, possibly damaging the devices and losing the connection. The stock lid in the Janis has a window so the connection can be made after the temperatures have reached an equilibrium meaning there would be no further thermal expansion or contraction. The new lid does not have a window making it extremely difficult to keep a connection with this method.

A Printed Circuit Board (PCB) was developed which would keep a stable electrical connection and hold the device in place. The PCB copper pads needed to precisely align with the devices' footprints, securely attach to the stage via screws, and provide a mechanism to connect to the probe arms. The 3D PCB model and the final deliverable can be seen in Figure 22.

Figure 22 Upper Left) Designed PCB in the 3D viewer in the KiCAD software. Upper Right) The manufactured PCB as it arrived.

This PCB design checked all these boxes. There are four large copper pads that have wires soldered to them which can be fed into the arms of the Janis. This creates a secure connection that will not fail due to thermal expansion or contraction. The devices were soldered onto the middle pads which followed the footprint given by the manufacturer. The devices were soldered with hot air and thermal paste as opposed to the typical hot iron soldering used for the wire connections.

The PCB was designed to be screwed to the Janis stage which gave great thermal contact so the device could operate at the desired temperature. There was concern that the introduction of the PCB would cause a temperature differential between the Janis thermocouples and the actual device. To check this, a Resistive Temperature Detector (RTD) was installed where the real devices would be. As seen in **Error! Reference source not found.**, the stage temperature measurement closely matched the temperature of the RTD. This confirmed that the PCB was not creating a dramatic difference between the stage and device temperature.

3.4 Tested Devices

Four different devices were tested during this experiment. There were three Indium Arsenide Antimonide (InAsSb) Hamamatsu photovoltaic detectors of varying bandgaps. The last was an Indium Gallium Arsenide (InGaAs) photodiode. Some device parameters can be found in Table 2 Table of parameters for the measure devices. The three Hamamatsu devices have the exact same packaging and footprint which the PCB was designed for. The GDP GAP 500 came in different packaging and required wire bonds to make the full circuit.

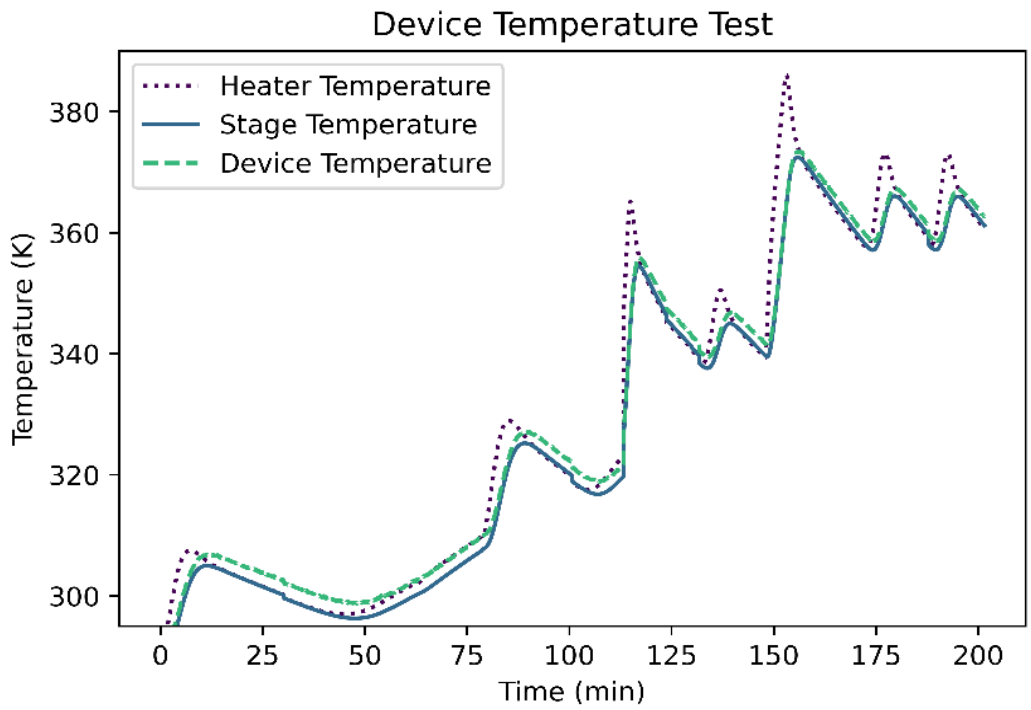

Figure 23 Temperature measurement of the internal Janus thermocouples along with an RTD mounted on the PCB to measure what the device temperature would be.

	GDP GAP 500	Hamamatsu P16612	Hamamatsu P16613	Hamamatsu P16614
Band edge (μm)	1.7	5	8	12
Bandgap (eV)	0.74	0.248	0.155	0.103
Area (m^2)	$1.96 \times 10^{-7}\ m^2$	$4.9 \times 10^{-7}\ m^2$	$4.9 \times 10^{-7}\ m^2$	$4.9 \times 10^{-7}\ m^2$

Table 2 Table of parameters for the measure devices.

The three Hamamatsu devices were soldered to the pads using a high melting point, low voiding solder CHIPQUIK Model No. SMD291SNL. The solder paste was deposited on the copper, where the device was then placed seen in Figure 24 Keyance images of the three Hamamatsu photovoltaic detectors. Upper Left) P16612 Upper Right) P16613 Lower) P16614. While holding the device with tweezers, a hot air gun was used to melt the solder and create the electrical connection between the device and the PCB copper pads.

The GDP GAP 500 has a different footprint as seen in Figure 25. As a result, the electrical connection could not be made in the same fashion. This device and its two contact pads are attached to a ceramic block with nothing on the backside. To connect this device electrically, the pads on the PCB were wire bonded to the pads on the device. Two wire bonds were used as a form of redundancy since these wires are extremely fragile. The ceramic block itself was glued to the solder mask of the PCB with silver paint.

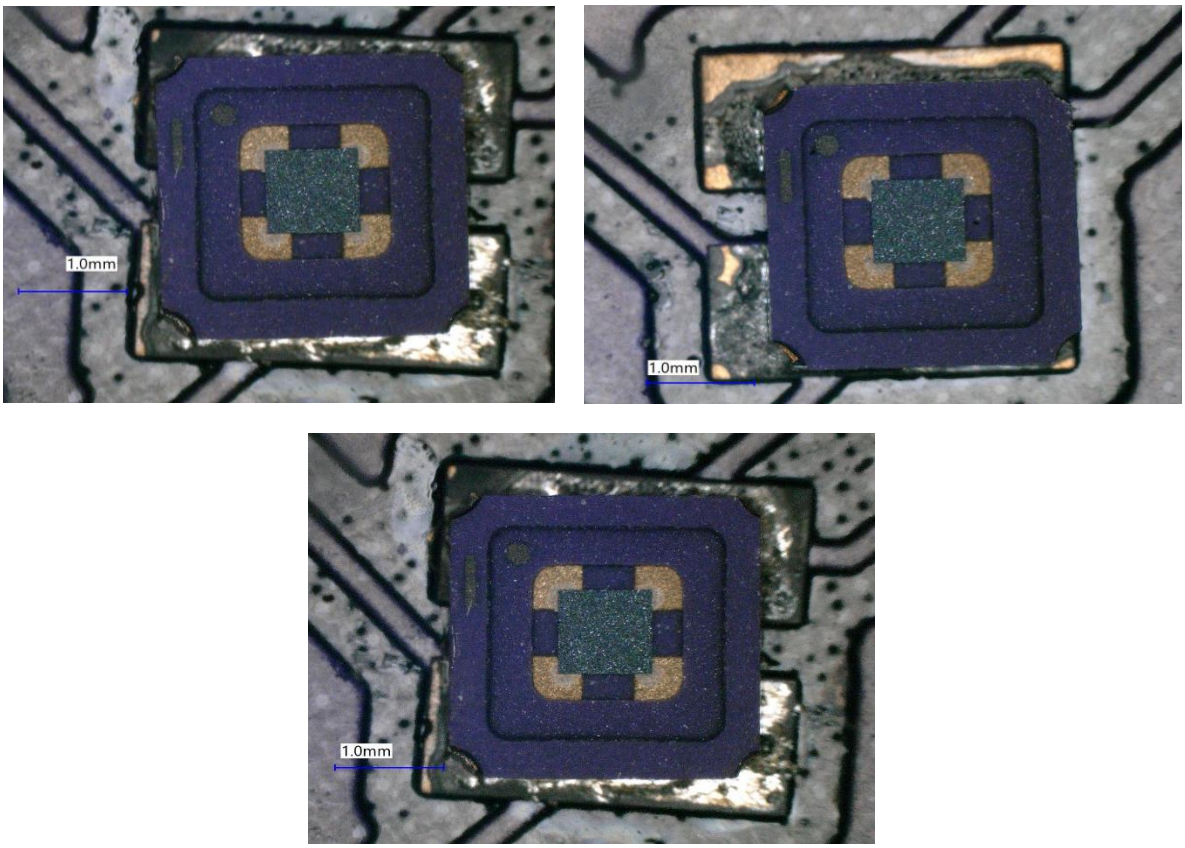

Figure 24 Keyance images of the three Hamamatsu photovoltaic detectors. Upper Left) P16612 Upper Right) P16613 Lower) P16614

3.5 Test Procedure and Parameters

Each run was completed using the same conditions and procedure to minimize any possible external effects on the data collection. The process used to prepare the experiment and run it is shown in Figure 27. The first step is to prepare the device by soldering it to the PCB and then installing the PCB onto the stage in the Janis.

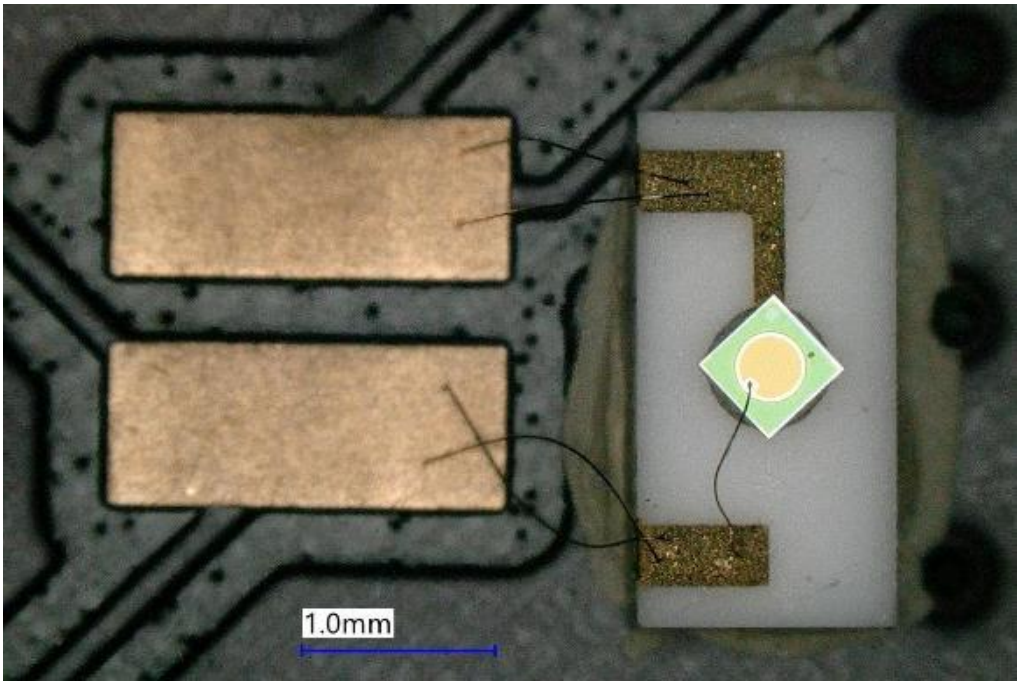

Figure 25 The device is on a small ceramic block with contact pads on top. The device is the circular yellow region. The device pads are wire bonded to the PCB pads.

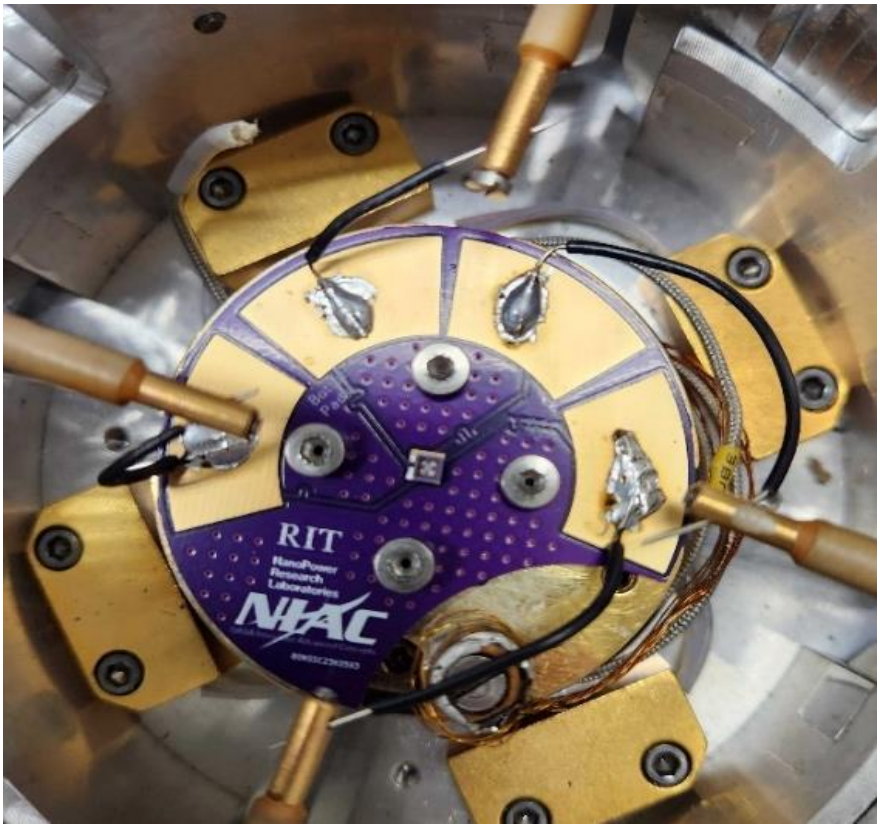

Figure 26 PCB with the device and connection wires soldered onto the pads which has been installed onto

Next, the chamber is pumped down until it reaches a minimum usually around $1 \times 10^{-5}\ mbar$. During the run this value may creep up to as high as $2.5 \times 10^{-4}\ mbar$ due to thermal contraction of the many O-rings in the system. Once the chamber is pumped down, liquid nitrogen can be poured into the lid to begin cooling. It is important to wait until the chamber has pumped down since the cooling of the lid will cause condensation to form wherever there is water vapor. This will quickly ruin a run and possibly damage the system if it happens inside the chamber.

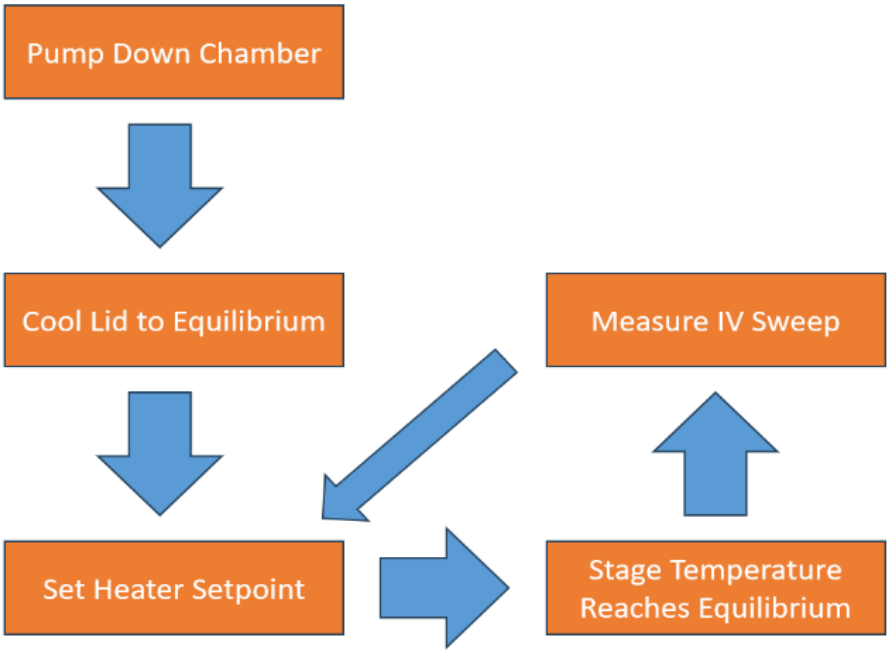

Figure 27 High level flow chart of the experiment process employed in this study.

After the lid is cooled to its equilibrium temperature of approximately 95 K, the main process loop can begin. First, the stage temperature setpoint is set and the Python script will wait until the temperature has been steady for an appropriate amount of time. The data collection is fast but not instant, so it is important that the stage temperature does not vary during the data collection. Once the stage temperature meets the steady state requirement, the voltage sweep can

begin. Once the voltage sweep is complete, the script moves the setpoint to the next temperature and the cycle is repeated until a stage temperature of 500 K is reached.

The voltage sweeps were conducted over a range appropriate to the device. For the Hamamatsu devices, this range was -70 V to 70 V with 1 mV steps. For the GDP GAP 500, this range was from -150 V to 100 V in 1 mV steps. The large range was picked to ensure the full power generating region was captured for each device. Within this large range, a smaller range was designated for higher resolution data collection. This region spanned 20 mV to 2 mV with step size of 10 µV for the Hamamatsu devices and -30 mV to 1 mV with a step size of 50 µV for the GDP GAP 500.

This change in step size allowed high resolution data to be collected in the region of interest without making the scan take an excessive amount of time. Since the region of interest is only a few mV wide, having high-resolution in this region is very important. If the 1 mV step was used for the whole scan, there would only be one or two points in the region of interest. Lastly, this measurement was taken in a four-wire sensing setup to reduce any resistance effects commonly found in two wire setups.

3.6 Results

This section will present the results from the experiment described above for each device. It is important to note that the Hamamatsu devices are not typical diodes, therefore the diode model does not necessarily apply to these devices. Due to the proprietary nature of these devices, their exact structure is not known which makes predicting their behavior difficult. First is the Hamamatsu P16614 InAsSb device which had the lowest bandgap energy of 0.103 eV. The top two plots in Figure 28 show the current and power curves versus voltage. In the current curves

there appears to be divot when a current density of 2 A/m^2 is reached. This is most likely not caused by the device itself but the auto-ranging of the Keithley 2400. This device portrayed some expected results.

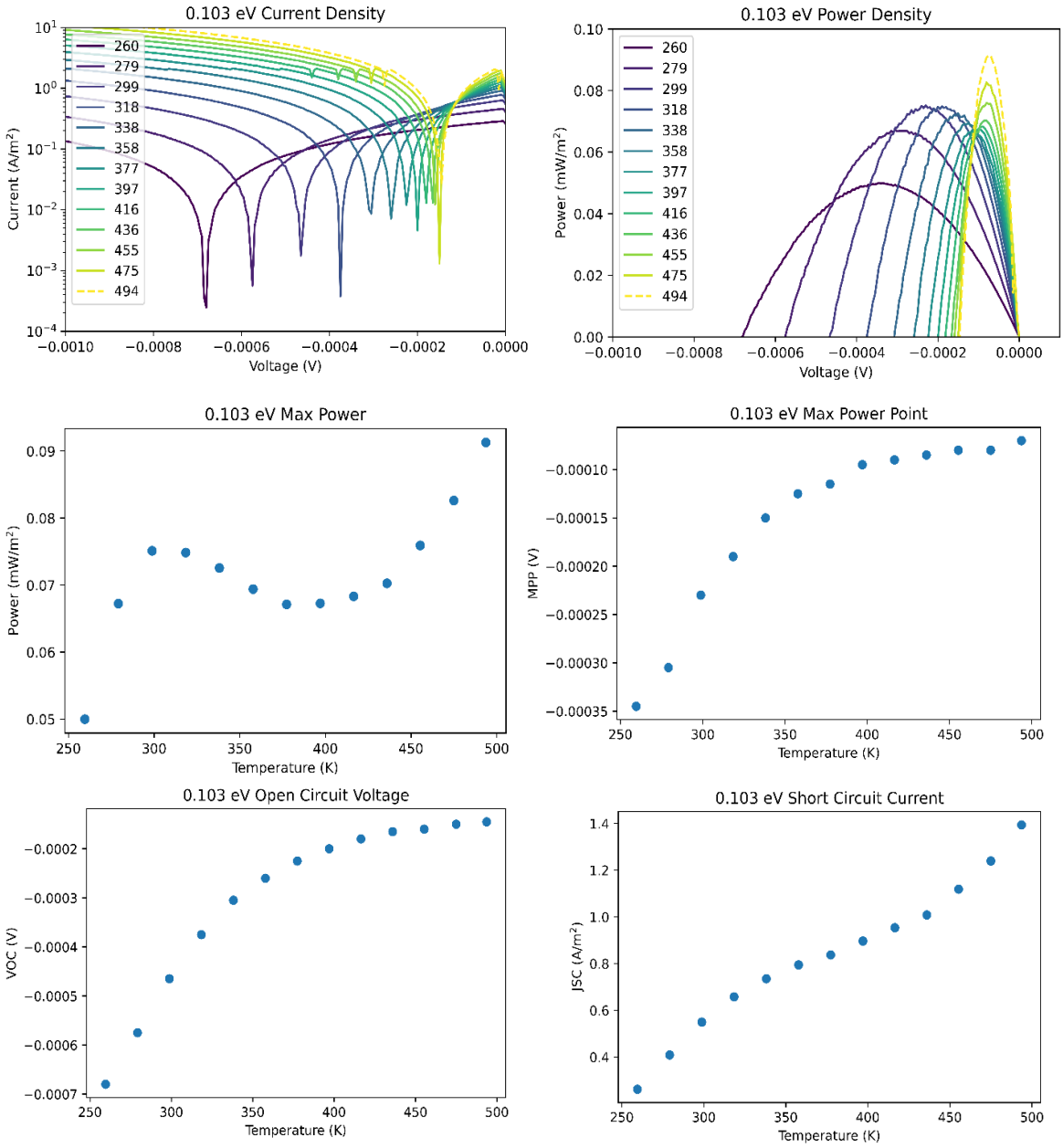

Figure 28 Results for the P16614 InAsSb Hamamatsu InAsSb 0.103 eV bandgap device. There are six plots showing different characteristics found from the measure IV curves.

First, the short-circuit current increased steadily with temperature. Additionally, the power also

increased with rising temperatures as well. The device performance was hindered by a dropping open-circuit voltage. This feature was common throughout all the tests in this study.

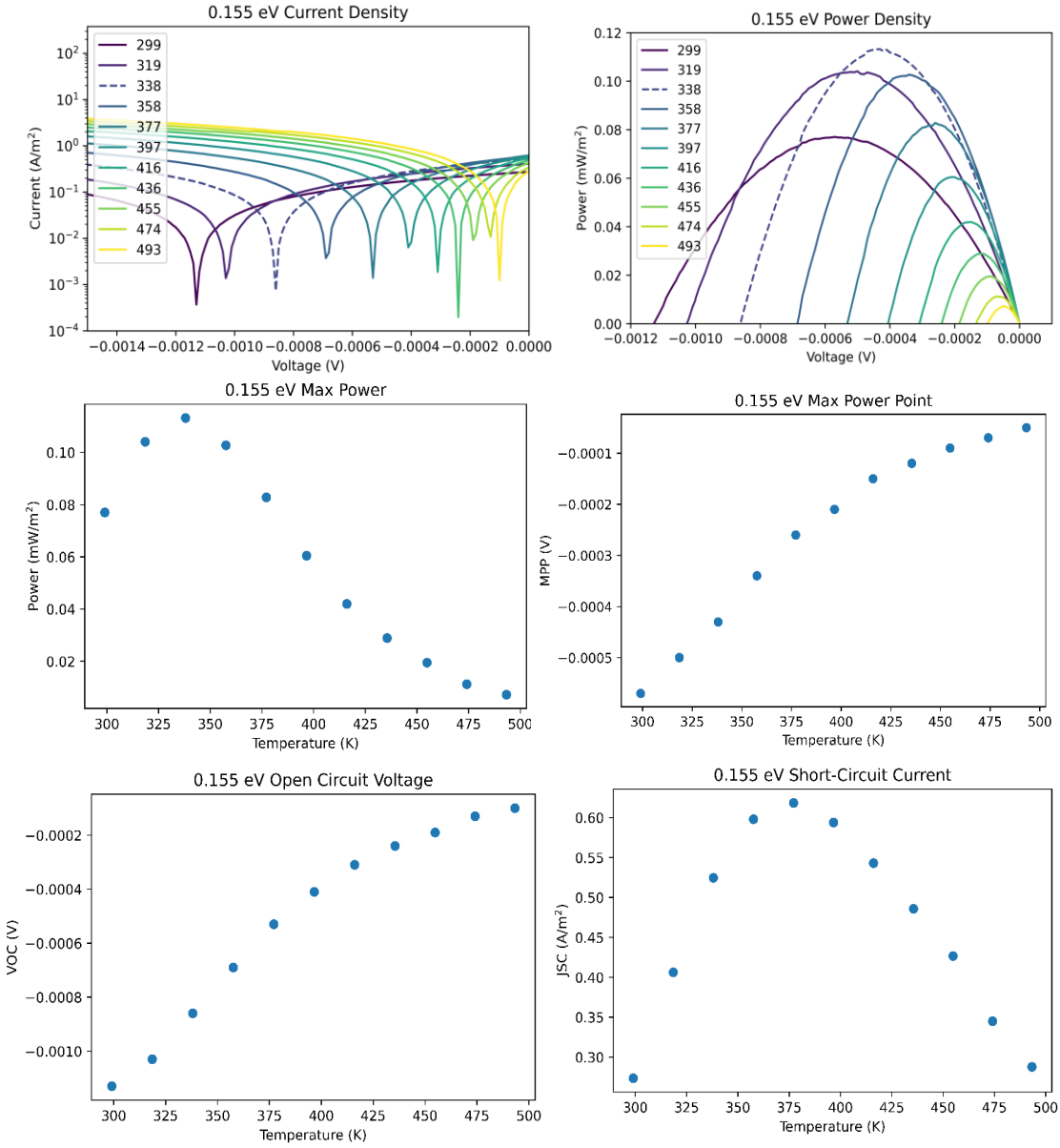

Figure 29 Results from the InAsSb Hamamatsu P16613 0.155 eV bandgap device.

P16613, the 0.155 eV Hamamatsu photovoltaic detector found in Figure 29 displays different features. Most notably, the short-circuit current began to decrease for temperatures

hotter than 375 K. This was unexpected, especially after the previous result. This device displayed the same trend of decreasing open-circuit voltage as temperature rises.

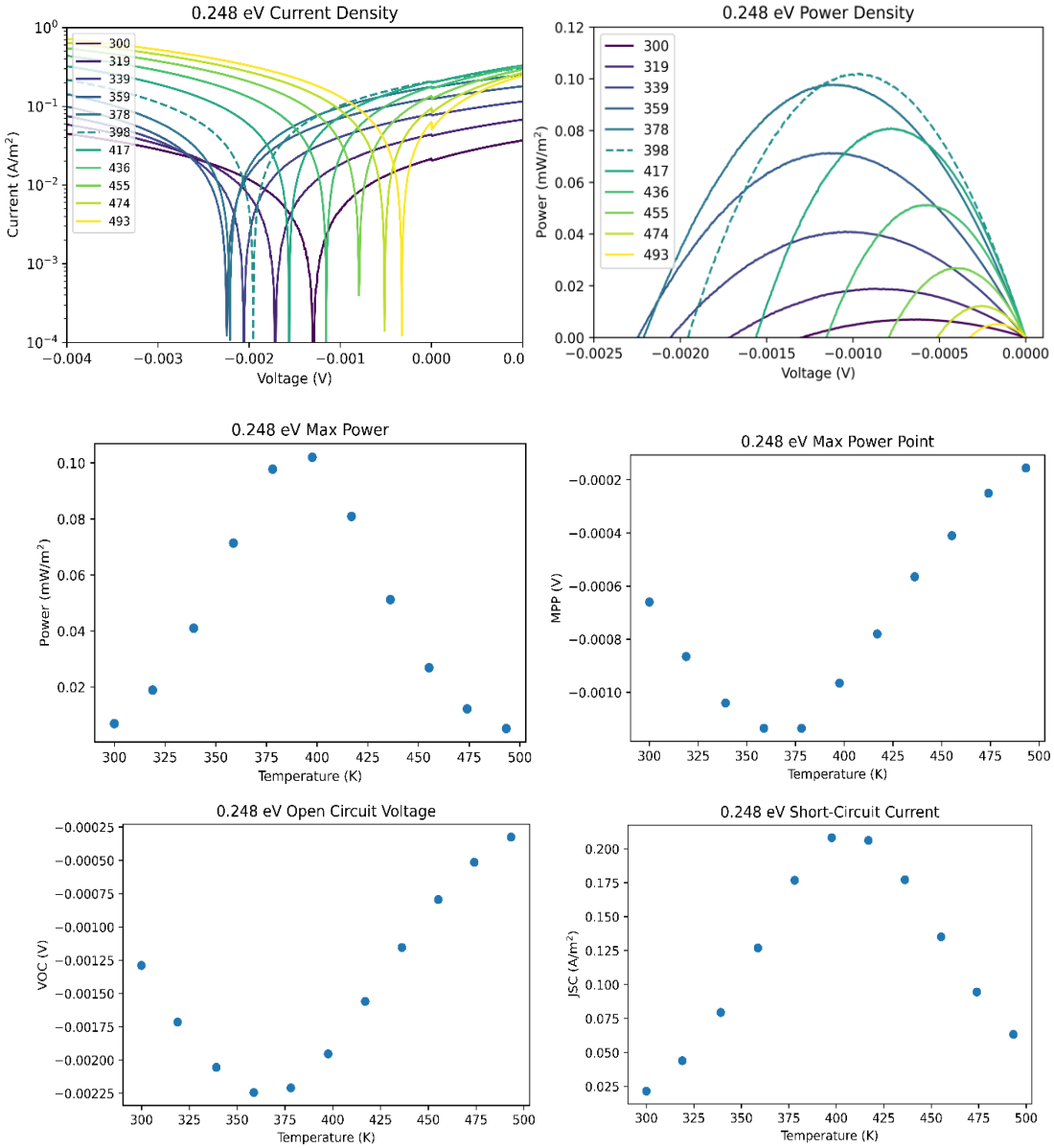

Figure 30 Results from InAsSb the Hamamatsu P16612 0.248 eV device.

The last Hamamatsu device with a bandgap of 0.248 eV displayed some of the same traits as the one before. The device characteristics are found in Figure 30. This device's short-circuit

current also began to drop as temperatures got too high. Unlike the others, the open-circuit voltage rose at low temperatures but began to fall again once the cell was above 350 K.

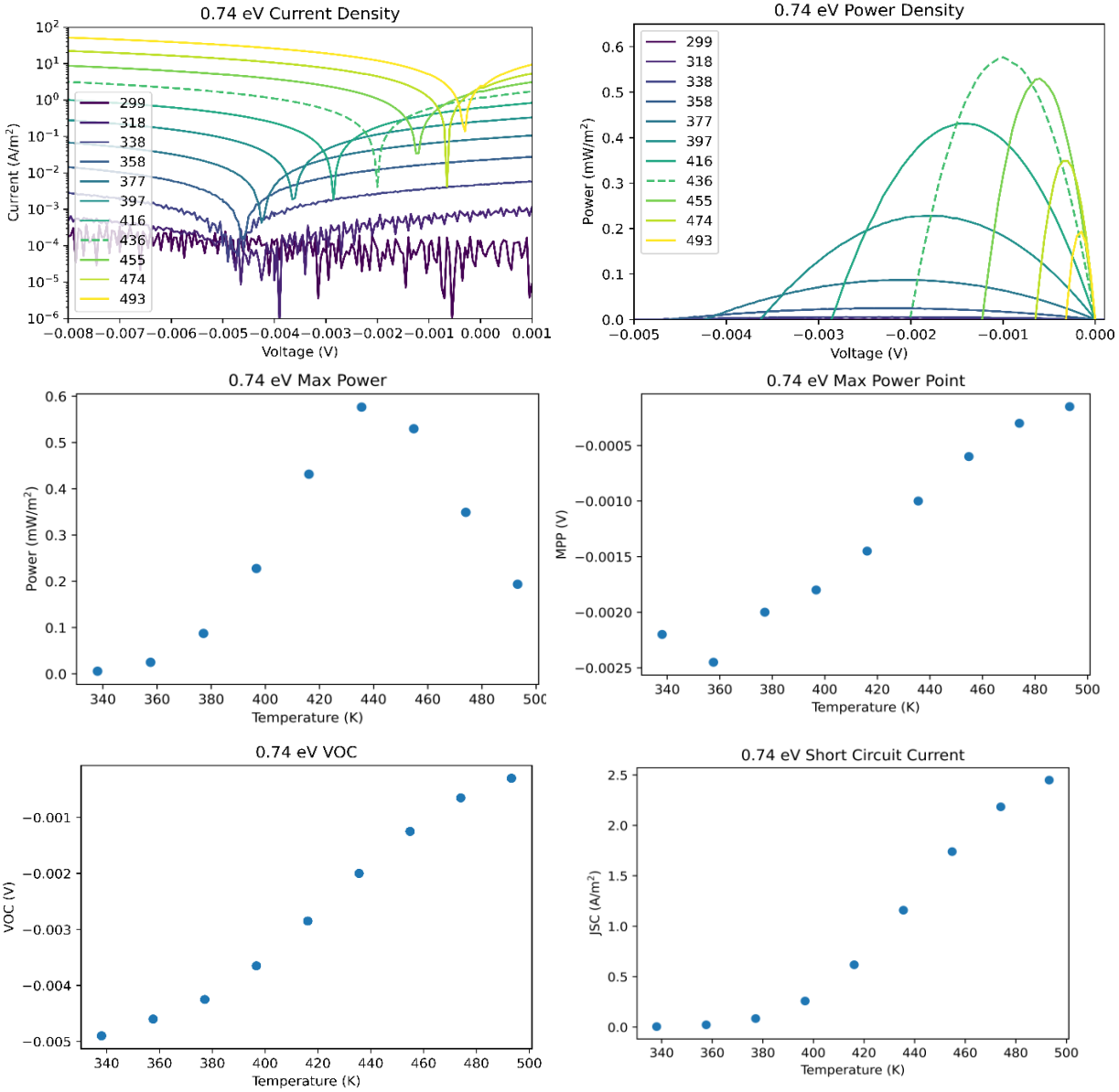

Figure 31 Results for the InGaAs 0.74 eV bandgap GDP GAP 500 device.

Finally, the InGaAs GDP GAP 500 photodiode displayed promising results. First it produced the highest power density at 0.59 $^{mW}/_{m^2}$ as seen in Figure 31. This is approximately 6x the max power density produced by the Hamamatsu devices. Additionally, this device showed

the expected increasing short-circuit current density that is expected from the theory. Despite these promising results, this device also suffered from the dropping open-circuit voltage found in the other device result.

Another notable aspect of these results are noisy current-voltage curves at low temperatures. The GDP GAP 500 produces a lower current overall due to its smaller active area. All measurement tools have a minimum sensitivity. If the values go below this floor, the tool will return only noise. Once the temperature rose to a high enough level, the current through the device was above this floor. Temperatures that produced noisy results were not included in the other results for this device.

4 Conclusions

4.1 Discussion

In short, all four devices demonstrated the thermoradiative effect by producing a measurable power, current and voltage. While these results are promising, other groups have produced more power with a smaller temperature difference using a HgCdTe diode [3]. This is unfortunate but gives much hope that there are a lot of possible optimizations when it comes to designing TRCs.

The models for loss mechanisms discussed in Chapter 2 had their effects combined to give a more descriptive picture. The material parameters of each device can be used as inputs into this model to will predict the power each device should produce. These values were obtained either from the specification sheet given by the manufacturer, or from material properties found in reference [15].

The final predictions for the power of the InGaAs photodiode can be found in Figure 32, with the material properties used to generate this plot found in Table 3. These values were used in Equation 13 to predict the power output of this device when Auger recombination, Shockley-Read Hall recombination, series, and shunt resistance losses were all considered. Since the SRH Lifetime and Radiative Recombination Coefficient are not always equivalent across devices, these values were altered to tune the model, so it best matched the experimental data. This analysis was completed for the measured temperature of 436 K since that temperature produced the maximum experimental power generation of $0.59 \times 10^{-5}\ {}^{mW}/_{cm^2}$.

Material Property	Value
Series Resistance	0.0018 Ω-cm^2
Shunt Resistance	1.6 MΩ
Electron Effective Mass	0.074M_0
Hole Effective Mass	0.363M_0
SRH Lifetime	$9 \times 10^{-6} s$
Auger Coefficient	$7 \times 10^{-29} \frac{cm^6}{s}$
Radiative Recombination Coefficient	$0.8 \times 10^{-7} \frac{cm^3}{s}$

Table 3 Table of material values used to calculate the power generation of the InGaAs photoidode.

Figure 32 shows a clear connection between the measured current vs. voltage curve and the modeled version. The model was able to be matched to the data verifying its validity and usefulness. The shunt resistance played the most important role in aligning the V_{oc}. The value given by the manufacturer aligned this parameter well. The radiative recombination coefficient was altered to match the magnitude of the power generation. The other parameters did not play as large of a role. For example, changing the auger recombination coefficient did not affect the model since the bandgap energy was high enough to keep the intrinsic carrier concentration low enough such that auger recombination was not a limiting factor. This will not be the case for lower bandgap devices.

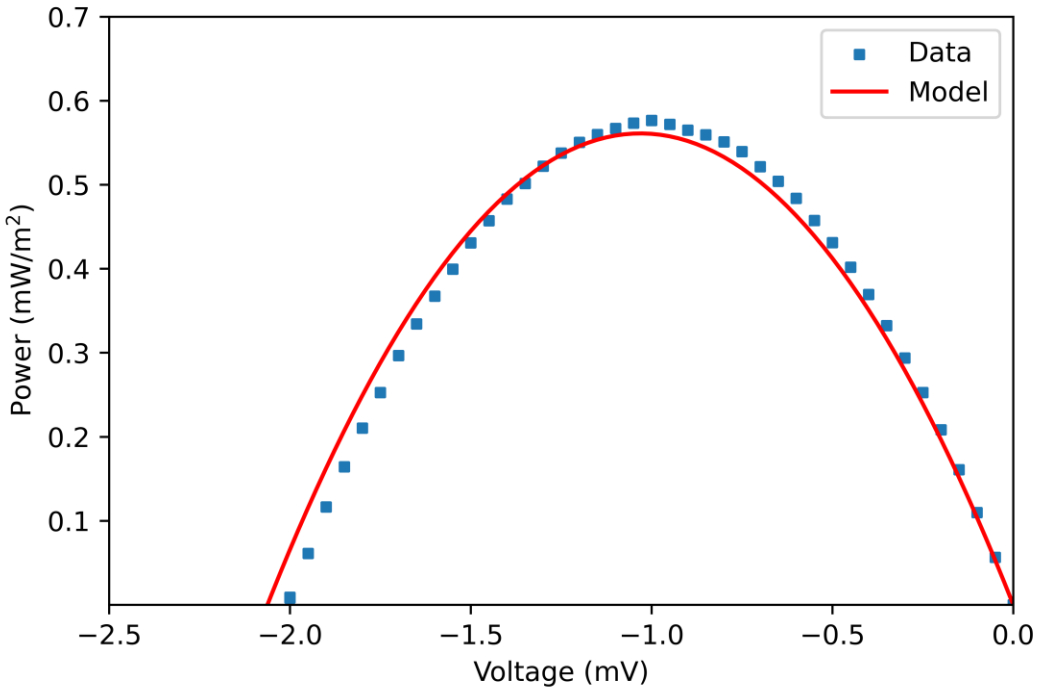

Figure 32 Simulated power curve for the InGaAs photodiode that includes all modeled loss mechanisms using the material properties for the devices tested in this study.

While these results are promising, there are some considerations to manage. First, empirically determined material properties are given for 300 K and can be sensitive to temperature changes which means these values may not be accurate at 500 K. Secondly, there may have been problems in the experimental setup. Despite its high temperature certification, the solder between the wires and the PCB pads had melted slightly in some runs. The connection was never completely broken but this still may have led to a change in the properties of the setup, which would influence the measured current versus voltage curves.

Lastly, the soldering of the devices onto the PCB may have damaged them. A high temperature solder paste was required since the experiment would run at a maximum temperature of 500 K. A typical solder past would melt long before this temperature was reached. This also meant that a very high solder temperature of 625 K was needed to fully melt

the solder paste to make the connection. The manufacturer recommends a solder temperature of about 515 K to be used only once. Heating the device over 100 K higher than its recommended temperature may have damaged the structure of the device which would dramatically increase non-ideality recombination rates. Additionally, the maximum recommended operating temperature is only 350 K. This experiment pushed this device far past its temperature limits both in the soldering and operation. These high temperatures may have permanently damaged the device, in turn reducing its overall output.

4.2 Future Work

In short, this study aimed to generate power using a TRC under spacelike conditions to determine the viability for its use in space power generation. The thermoradiative process was demonstrated for space conditions both experimentally and theoretically. The calculations seen in Chapter 2 clearly demonstrated that TRCs will theoretically produce power. Chapter 3 & Chapter 4 showed that a diode under TRC conditions will generate usable electrical power. These results were convincing enough for this group to be awarded a very selective NIAC Phase II program.

There are many ways to improve this study given more time and resources. First, completing the same measurement with a HgCdTe diode would be useful. Since many other groups use this type of device, this measurement would allow comparison between this setup and that of other researchers. This measurement would also be enlightening for the community since no group has used such a large temperature delta in their experiments.

Secondly, designing a structure meant to be used as a TRC and able to handle the high temperatures would shine more light on the potential of this device. This would involve growing

the material in-house with the NPRL MOCVD and fabricating these wafers into devices in the Semiconductor Nanofabrication Laboratory. Designing and fabricating a device specifically as a TRC would allow a researcher to tailor the structure to the needs of the project, something that is not possible when buying devices off the shelf.

The simulation model could be improved by using measurements made on the grown material instead of using value provided in the literature. This would give more certainty in the material constants which means any discrepancies are a result of the model itself and not the inputs. This would allow more tailored modifications which will increase its accuracy. Additionally, many of these material parameters have not been measured for high temperatures, which could be another area of study. Along with this, determining the upper limit device temperature will be crucial to maximize the device output without damaging the material.

Lastly, the experimental procedure can be updated to reduce possible external factors from altering the measurement. The Janis Cryostat worked well, but for a longer study a more permanent and reliable setup will be needed. This could include repurposing the Space Chamber in the Nano-Power Research Lab's (NPRL) arsenal to fit the needs of this project. Additionally, finding a way to create the electrical connection without having to use solder paste would reduce potential damage to the devices.

References

[1] National Aeronautics and Space Administration, "Multi-Mission Radioisotope Thermoelectric Generator (MMRTG)," 18 May 2020. [Online]. Available: https://science.nasa.gov/planetary-science/programs/radioisotope-power-systems/.

[2] R. Strandberg, "Theoretical efficiency limits for thermoradiative energy conversion," *Journal of Applied Physics,* 2015.

[3] M. Nielson and J. Ekins-Daukes, "Thermoradiative Power Conversion from HgCdTe Photodiodes and," *ACS Photonics,* 2022.

[4] M. Ono, P. Santhanam and S. Fan, "Experimental demonstration of energy harvesting from the sky using the negative illumination effect of a semiconductor photodiode," *Applied Physics Letters,* 2019.

[5] P. Santhanam and S. Fan, "Thermal-to-electrical energy conversion by diodes under negative illumination," *Physical Review B,* 2016.

[6] L. Chungwei, "Performance comparison between photovoltaic and thermoradiative devices," *Journal of Applied Physics,* 2017.

[7] D. V. Schroeder, An Introduction To Thermal Physics, Addison-Wesley, 2000.

[8] W. Shockley and H. J. Queisser, "Detailed Balance Limit of Efficiency of p-n Junction Solar Cells," *Journal of Applied Physics,* 1961.

[9] A. D. Vos and H. Pauwels, "On the Thermodynamic Limit," *Journal of Applied Physics,* 1981.

[10] J. D. Phillips, "Thermoradiative Cell Equivalent Circuit Model," *IEEE Transactions on Electron Devices,* 2021.

[11] A. V. Von Arx, "MMRTG Heat Rejection Summary," in *AIP Conference Proceedings*, 2006.

[12] N. F. Mott, "Recombination; a survey," *Solid-State Electronics,* 1978.

[13] J. D. Phillips, "Evaluation of Auger Limited Behavior in Thermoradiative Cells," in *2022 IEEE 49th Photovoltaics Specialists Conference (PVSC)*, 2022.

[14] H. Masui, Introduction to the Light Emitting Diode, Springer, 2023.

[15] Ioffe Institute, "Semiconductors on NSM," [Online]. Available: https://www.ioffe.ru/SVA/NSM/Semicond/..

[16] B. G. Streetman and S. K. Banerjee, Solid State Electronic Devices 7th Edition, Upper Saddle River: Pearson Education, 2015.

[17] S. Krishnamurthy and M. A. Berding, "Full-band-structure calculation of Shockley–Read–Hall recombination rates in InAs," *Journal of Applied Physics,* 2001.

[18] T. Deppe and J. N. Munday, "Nighttime Photovoltaic Cells: Electrical Power Generation by Optically Coupling with Deep Space," *ACS Photonics,* 2020.

[19] W.-C. Hsu, "Entropic and Near-Field Improvements of Thermoradiative Cells," *Scientific Reports,* 2016.

[20] E. J. Tervo, "Solar Thermoradiative-Photovoltaic Energy Conversion," *Cell Reports Physical Science,* 2020.

[21] X. Zhang, "Parametric design criteria of an updated thermoradiative cell operating at optimal states," *Journal of Applied Physics,* 2017.

[22] X. Zhang, "Thermodynamic limits and performance optimization of nighttime thermoradiative energy conversion systems with non-idealities," *Case Studies in Thermal Engineering,* 2023.

[23] T. H. Gfroerer, "Recombination in Low-Bandgap InGaAs," in *2006 IEEE 4th World Conference on Photovoltaic Energy Conference*, 2006.

[24] J. Li and L. Chen, "Exergoeconomic performance optimization of the space thermoradiative cell," *The European Physical Journal Plus,* 2021.